

## Simulated Changes in Atmospheric Transport Climate

MARK HOLZER\* AND GEORGE J. BOER

*Canadian Centre for Climate Modelling and Analysis, Meteorological Service of Canada, University of Victoria,  
Victoria, British Columbia, Canada*

(Manuscript received 27 December 2000, in final form 1 June 2001)

### ABSTRACT

Atmospheric “transport climate” characterizes how trace gases are distributed by and within the atmosphere, on average, as a consequence of the interaction of atmospheric flow with tracer sources and sinks. The change in transport climate under global warming is investigated using passive tracers. Experiments with constant localized surface sources, pulsed sources, and pulsed boundary conditions are analyzed using a Green-function approach in conjunction with a climatological budget calculation.

Under climate warming, interhemispheric exchange times, mixing times, and mean transit times all increase by about 10%. The main transport pathway between the hemispheres via the “tracer fountain” at the ITCZ is suppressed. Generally less vigorous flow manifests itself in higher tracer burdens in the source hemisphere and in downwind plumes of enhanced mixing ratio close to the sources; these increases are also about 10%. Resolved advection and subgrid transport do not cooperate for all sources in enhancing the near-source mixing ratio. The warmer climate has a reduced cross-tropopause gradient, primarily due to a slightly higher tropopause, which results in a reduction of about 25% in the average tropospheric tracer mixing ratio, and a corresponding enhancement in the stratosphere. A global variance budget shows increased mean and transient tracer variance due to increased generation from strengthened mean gradients near the source and weakened eddy and subgrid transport.

### 1. Introduction

The instantaneous state of the climate system is specified by many fields including the familiar ones of temperature, pressure, velocity, and precipitation rate. The statistics of these quantities determine the climate. In this sense, the statistics of tracer mixing ratio in the atmosphere (and ocean) constitute the tracer climate. The climate of a passive tracer also characterizes the transport climate since it depends on, but does not affect, the transport properties of the flow. Large-scale atmospheric transport will change as a consequence of global climate change. This will alter the distribution of long-lived trace gases and the dispersal of pollutants, and have implications for their environmental impact. In this paper, we study the effect of climate change on transport using the Canadian Centre for Climate Modelling and Analysis’s (CCCma) coupled global climate model (Flato et al. 2000) and the results of transient climate change

simulations (Boer et al. 2000a,b). The atmospheric component of the CCCma model (McFarlane et al. 1992) is used to perform separate simulations of passive tracer transport for the present climate and for the future climate projected for the late twenty-first century. Appropriate sea surface temperatures (SSTs) and corresponding greenhouse-gas-plus-aerosol radiative forcing are specified from the archived data of the transient simulations. Tracer sources and boundary conditions are prescribed to be identical for the present and future climates so that changes in tracer distribution are due only to changes in transport.

Changes in tracer transport and distribution are investigated in terms of interhemispheric exchange times, transit-time distributions, and mixing times. A Green-function approach (Holzer 1999) provides insight into how the change in equilibrium tracer distribution is attained and a variance budget into how the changed structures are maintained.

### 2. Experimental design

We perform three sets of experiments to probe changes in atmospheric transport climate. Two are aimed at understanding changes in the distribution and transport of passive tracers from specific source locations. A third investigates changes in the probability distribution of tropospheric transit times.

---

\* Current affiliation: Department of Earth and Ocean Sciences, The University of British Columbia, and Physics Department, Langara College, Vancouver, British Columbia, Canada.

---

*Corresponding author address:* Dr. Mark Holzer, Department of Earth and Ocean Sciences, The University of British Columbia, 6339 Stores Rd., Vancouver, BC V6T 1Z4, Canada.  
E-mail: mholzer@langara.bc.ca

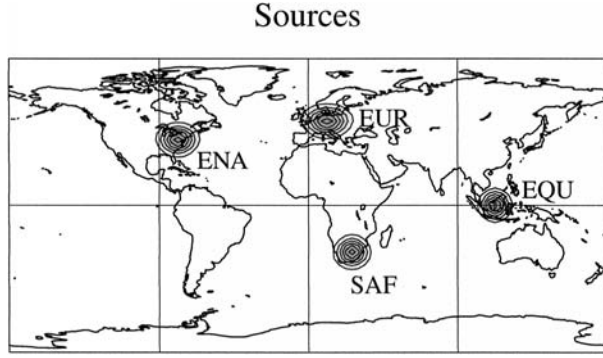


FIG. 1. The four localized sources: Europe (EUR, 50.1°N, 11.3°E), eastern North America (ENA, 39.0°N, 78.3°W), equatorial (EQU, 0°N, 113°E), and South Africa (SAF, 27.8°S, 26.3°E). All sources have the same Gaussian shape (differences in appearance are due to map projection).

#### a. Stationary-state experiments

The continuity equation for the mass mixing ratio  $\chi$  of a passive tracer is

$$\partial_t \chi + \mathcal{T}(\chi) = S, \quad (1)$$

where  $\partial_t \equiv \partial/\partial t$  and  $\mathcal{T}$  is the linear transport operator representing advection and diffusion. The first set of experiments simulates tracer distributions from surface sources  $S$  that are constant in time, so that changes in mixing ratio are due only to changes in the flow and not to any changes in sources or sinks. For surface sources the vertical integral,  $\int_0^{p_s} S dp/g \equiv \phi$ , is the effective tracer surface mass flux ( $p_s$  is surface pressure;  $g$  is acceleration of gravity). In practice, surface sources inject tracer into the lowest model level and zero-flux boundary conditions (BCs) are enforced at the surface.

With  $S$  constant,  $\chi = \chi^0 + \chi^+$  reaches a quasi-equilibrium state consisting of a spatially uniform background mixing ratio  $\chi^0$ , which increases linearly in time, and a statistically stationary, spatially varying component  $\chi^+$ . Physically,  $\chi^0(t) = M(t)/M_A$ , where  $M(t)$  is the instantaneous total tracer mass,  $M_A$  is the mass of air in the atmosphere, and the mass-weighted global integral  $\int_{M_A} \chi^+ dM = 0$ . The equation for  $\chi^+$  follows from (1) as

$$\partial_t \chi^+ + \mathcal{T}(\chi^+) = S - \Sigma, \quad (2)$$

where  $\Sigma \equiv \partial_t \chi^0$ . From the definition of  $\chi^0$  it follows that

$$\Sigma = g \langle \phi \rangle / \langle p_s \rangle, \quad (3)$$

where the  $\langle \rangle$  in (3) denote the global horizontal area-weighted average. The spatially uniform sink  $\Sigma$  balances the nonuniform source  $S$  when globally integrated, that is,  $\int_{M_A} (S - \Sigma) dM = 0$ . Thus,  $\chi^+$  does not have net sources or sinks as required since  $\int_{M_A} \chi^+ dM = 0$ .

We investigate changes in “transport climate” for tracers from the four surface sources shown in Fig. 1. The

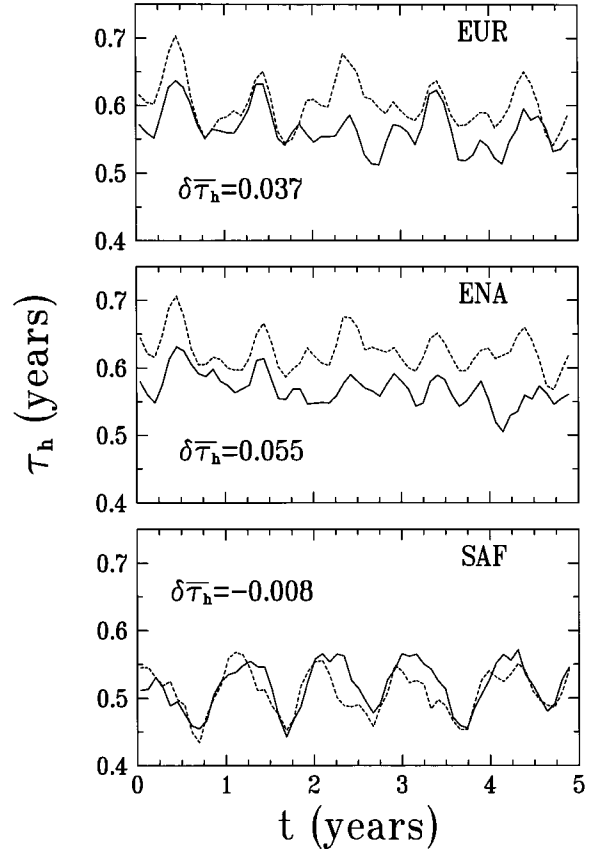


FIG. 2. The interhemispheric exchange time  $\tau_h$ , averaged over 30 days, for the sources indicated. Solid lines correspond to current, and dashed lines to future, conditions. The change in the average value of  $\tau_h$  is indicated as  $\delta \bar{\tau}_h$ , in years.

choice of localized (rather than distributed) sources permits the identification of transport pathways from definite locations. Moreover, the sources of many real tracers [e.g.,  $\text{SF}_6$ , chlorofluorocarbons (CFCs)] are similarly localized. Transport of tracer from the Europe (EUR) and eastern North America (ENA) sources has been previously investigated in some detail for current climate conditions (Holzer 1999). The choice of the equator (EQU) and South Africa (SAF) sources is not motivated by current or projected real tracer sources, but aims to probe atmospheric transport changes in regions of convection (EQU) and to explore hemispheric asymmetry in transport climate change (SAF). All sources have a Gaussian shape  $\phi \propto \exp[-(r/r_0)^2/2]$ , where  $r$  is the geodesic distance from the pattern center, with the choice  $r_0 = 2\pi a/70 = 572$  km ( $a$  is the earth's radius).

For each constant source, (1) is integrated as part of GCMII (i.e., online) for the periods 1990–2000 and 2090–2100, with separate runs for each period. Tracer mixing ratio is initialized to zero at the beginning of each run, so that for the same integration time, the 1990–2000 simulation holds exactly the same tracer mass as the 2090–2100 simulation. Consequently,  $\delta \chi^0 = 0$  so

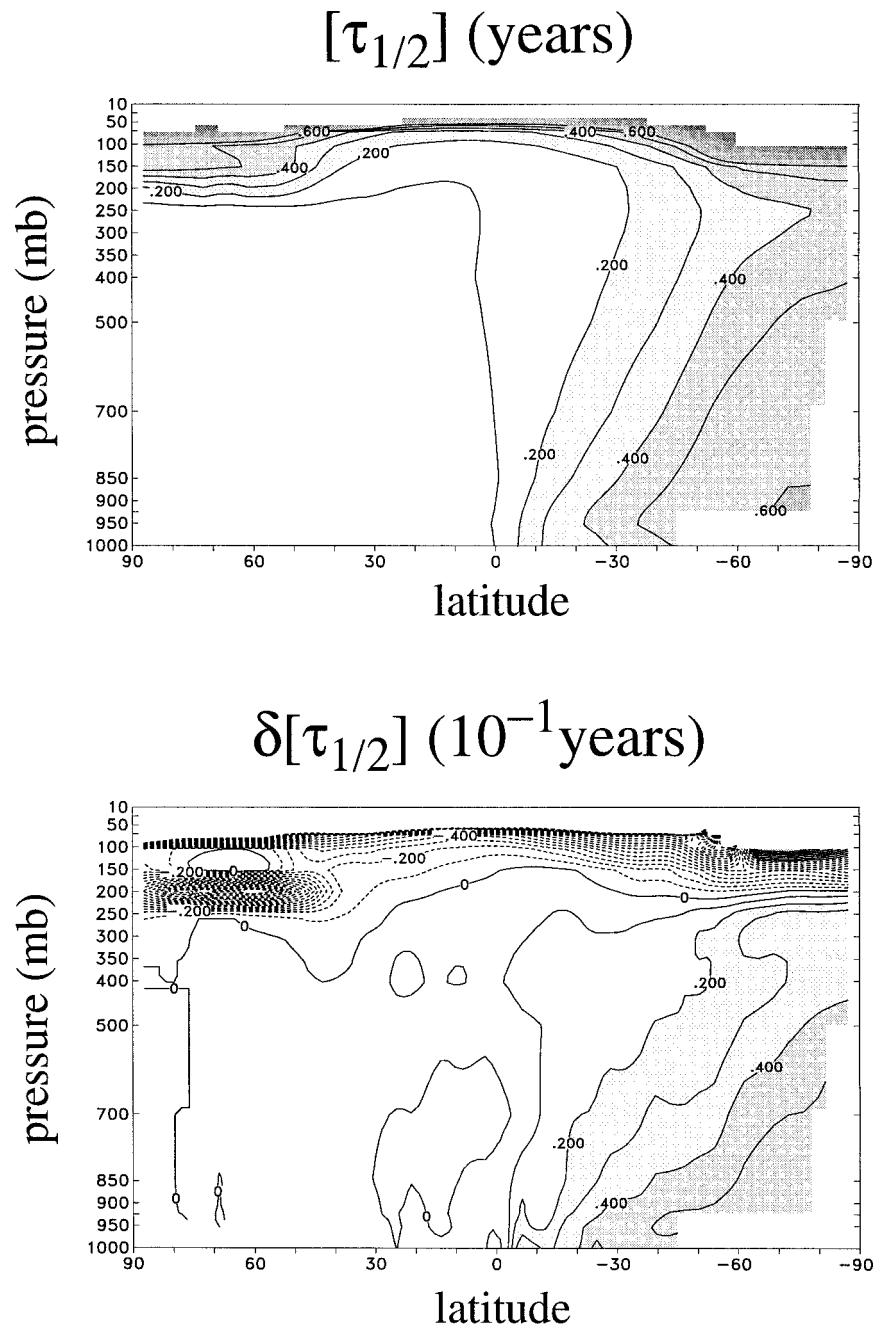


FIG. 3. (top) The annually and zonally averaged time,  $[\tau_{1/2}]$ , for  $G$  to reach 1/2 of its asymptotic value of  $G_{\infty}$  for the current climate, and (bottom) the change  $\delta[\tau_{1/2}]$  for a warmer climate for the ENA source.

that  $\delta\chi = \delta\chi^+$ . (Throughout, we will use the notation  $\delta X \equiv X_{\text{future}} - X_{\text{current}}$  to denote the difference in some quantity  $X$  between the runs for the future and current climates, so that  $\delta X$  represents the change in  $X$  under global warming.) Here,  $\chi^+$ , and not  $\chi$ , is the variable used for diagnostics, because of its statistical stationarity at long times. Climatological monthly averages are calculated for the last five years of the simulations. (Four

years is long enough for transient behavior to have decayed so that  $\chi^+$  is statistically stationary in the troposphere).

The transport operator  $\mathcal{T}$  may be represented as the sum of the advection by the model's resolved winds and the vertical transport by parameterized processes. For diagnostic calculations we use pressure  $p$  as the vertical coordinate and write  $\mathcal{T}$  in flux form as

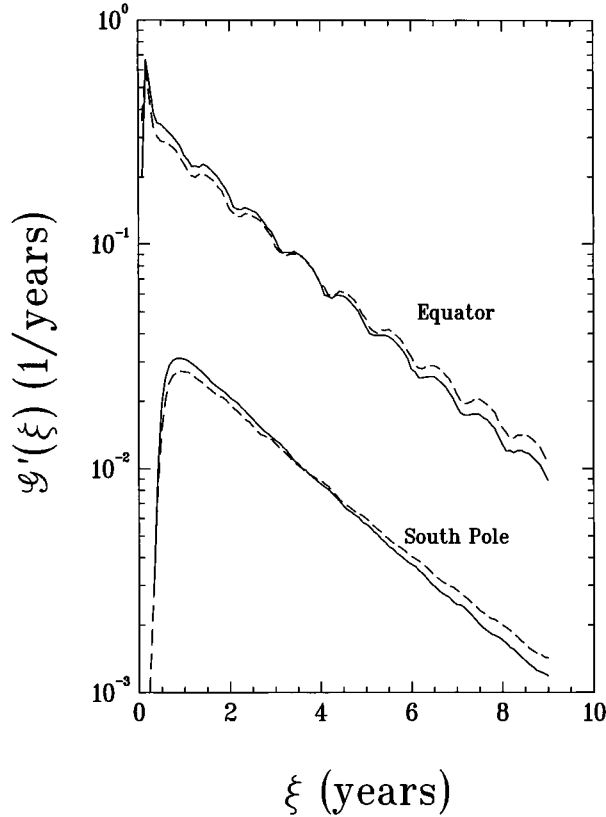


FIG. 4. The probability density functions (pdfs)  $G'(\xi)$ , of transit times  $\xi$  since an air parcel at the lowest model level, at the equator or at the South Pole, last had contact with the 45°N polar cap during Jan of year 0. The pdfs have been zonally averaged. The solid (dashed) lines are the pdfs for the current (future) climate and the equator curves have been shifted vertically for clarity.

$$\mathcal{T}(\chi) = \nabla \cdot (\mathbf{V}\chi) + \partial_p(\omega\chi) - \mathcal{D}(\chi), \quad (4)$$

where  $\mathbf{V} \equiv (u, v)$  is horizontal velocity and  $\omega = dp/dt$  is the vertical “pressure velocity.” Horizontal parameterized transport is small compared to the other terms and is neglected so that  $\mathcal{D}$  represents the transport due to parameterized vertical convection and diffusion. We may regard  $\mathcal{D}$  as the convergence of an effective vertical subgrid flux  $f$ , that is,  $\mathcal{D} = -g\partial_p f$ . Because surface fluxes are treated as internal sources in the lowest layer,  $f(p_s) = f(0) = 0$  and  $\int_0^{p_s} \mathcal{D} dp = 0$ .

In these experiments a change in atmospheric flow implies a spatial redistribution of tracer mass. The climatological balance is  $\partial_t \bar{\chi} + \mathcal{T}(\bar{\chi}) = S - \Sigma$ , where the overbar indicates a long-time average. Since  $\partial_t \bar{\chi}$  is small and since, by design,  $\delta(S - \Sigma) = 0$ , the change in transport climate must satisfy  $\delta \mathcal{T}(\chi) \approx 0$ . Because  $\mathcal{T}(\chi)$  represents the three-dimensional divergence of the total (that is, resolved plus subgrid) tracer flux as in (4), changes in these tracer fluxes must be nondivergent. While specifying  $S$  to be the same in the current and future climates ensures that any changes in mixing ratio are only due to changes in the flow, the constancy of

TABLE 1. Percentage changes of the average tropospheric ( $\chi_t$ ) and stratospheric ( $\chi_s$ ) mixing ratios and the first-order contributions to these from changes in strat–trop exchange time  $\tau$  and in troposphere fraction  $\alpha$  as given by (13). All quantities are annually averaged.

	Mixing ratios	Exchange time	Tropospheric fraction
Tropospheric	–27.5%	–6.16%	–25.6%
Stratospheric	+16.6%	+6.16%	+10.6%

the sources constrains the transport so that the divergent fluxes cannot change. This constraint highlights the subtlety of the problem of identifying changes in tracer distribution with changes in the flow.

### b. Green-function experiments

The statistically stationary mixing ratio  $\chi^+$  resulting from a constant source may be considered as the linear superposition of the mixing ratios resulting from a continuous sequence of pulses from that source. Our second set of experiments simulates the evolution of tracer from individual pulses. The normalized mixing ratio from a single pulse of a localized source is the coarse-grained Green function  $G$  associated with (1) for that source location (Holzer 1999). For the localized source  $S(\mathbf{r})$ , the corresponding coarse-grained  $G$  is the solution of

$$(\partial_t + \mathcal{T})G_m(\mathbf{r}, t) = S_\delta(\mathbf{r})\Delta_m(t), \quad (5)$$

where  $S_\delta(\mathbf{r})$  is  $S(\mathbf{r})$  scaled so that it integrates to unity over the mass of the atmosphere, that is,  $S_\delta = S/\int_{M_A} S dM$  and  $\Delta_m(t)$  is a square pulse of a 1-month duration,  $\Delta t$ , and amplitude  $1/(\Delta t)$ . Zero-flux BCs are applied to (5) as for (1), so that with increasing time  $G$  is spread uniformly over the entire atmosphere to the limiting constant  $G_\infty = 1/M_A$ . Note that  $G$  has dimensions of inverse mass.

We think of  $S_\delta$  and  $\Delta_m(t)$  as broadened Dirac  $\delta$ -functions. The subscript  $m$ , which labels the month for which the source is “on,” is the discretized analog of the source time  $t'$  and the location of  $S_\delta$  is the analog of the source point  $\mathbf{r}'$ , in the usual continuous definition of  $G(\mathbf{r}, t | \mathbf{r}', t')$  as the response to  $\delta(\mathbf{r} - \mathbf{r}')\delta(t - t')$  [see, e.g., Morse and Feshbach (1953) for a comprehensive discussion on Green functions]. In this paper, we consider only monthly means and denote the monthly mean of  $G_m(\mathbf{r}, t)$  over month  $n$  by  $G_{n,m}(\mathbf{r})$ . The quantity  $G_{n,m}(\mathbf{r})$  is the discrete analog of  $G(\mathbf{r}, t | \mathbf{r}', t')$  with the indices  $n$  and  $m$  playing the roles of  $t$  and  $t'$ . Since we do not compute  $G$  for all possible source locations  $\mathbf{r}'$ , we can only use  $G_{n,m}(\mathbf{r})$  to synthesize tracer from a source with the same location as  $S_\delta$ . (Computation of the complete  $G$ , that is, the response to a delta function source for all possible source points  $\mathbf{r}'$  and source times  $t'$  is practically impossible even for a GCM of modest resolution.) Thus, arbitrary, nonuniform initial conditions  $\chi(\mathbf{r}, t_0)$  cannot be propagated forward in time



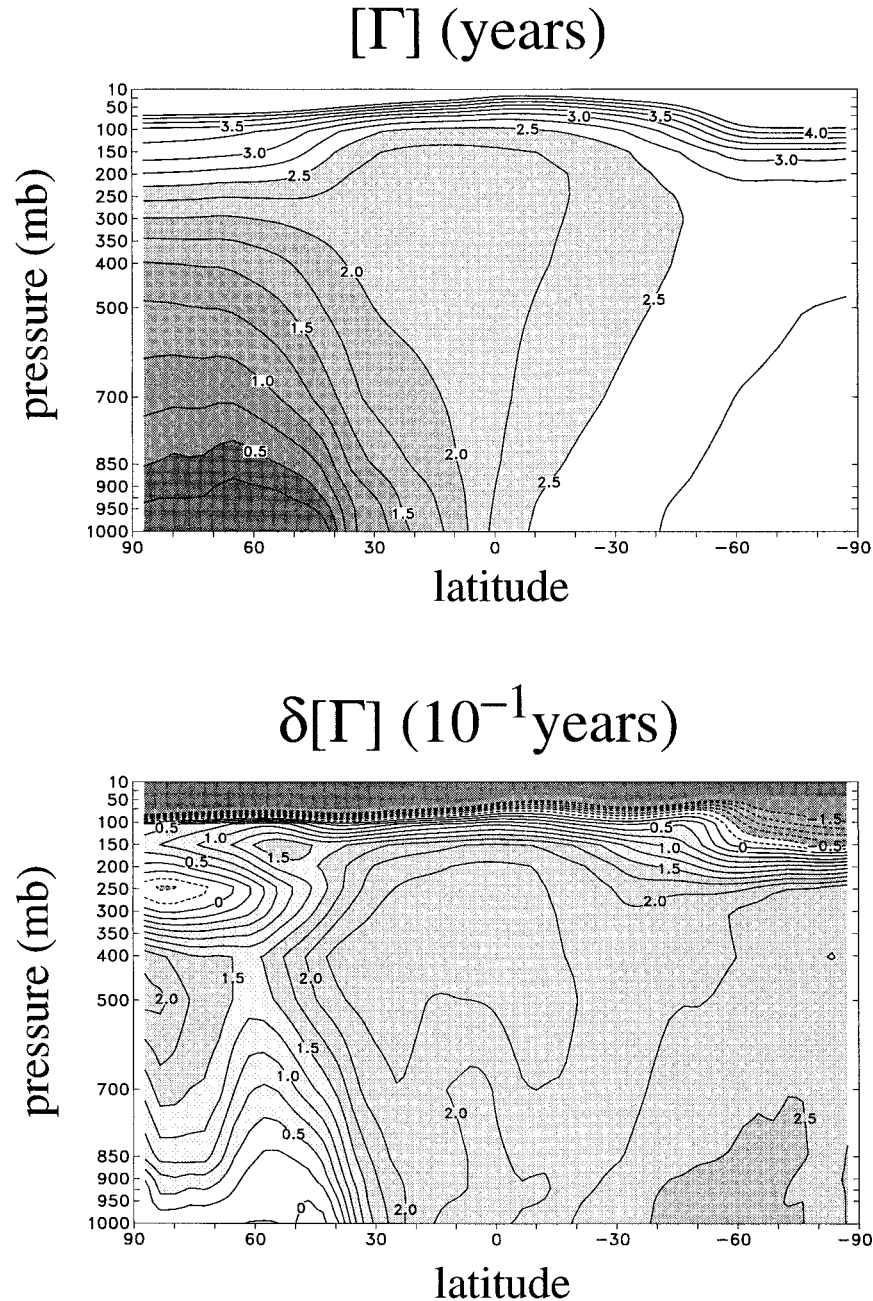


FIG. 5. Zonally and annually averaged mean transit time  $[\Gamma]$  since last contact with the  $45^\circ\text{N}$  polar cap. The top panel shows  $[\Gamma]$  under current climate conditions, while the bottom panel shows the change  $\delta[\Gamma]$  under global warming.

using  $G_{n,m}(\mathbf{r})$  through an analog of the spatial convolution  $\chi(\mathbf{r}, t) \sim \int G(\mathbf{r}, t | \mathbf{r}', t_0) \chi(\mathbf{r}', t_0) d^3 r'$ . We, therefore, consider only zero initial conditions, or equivalently imagine waiting sufficiently long for the contribution of any initial mixing ratio to have been uniformly mixed to a structureless offset.

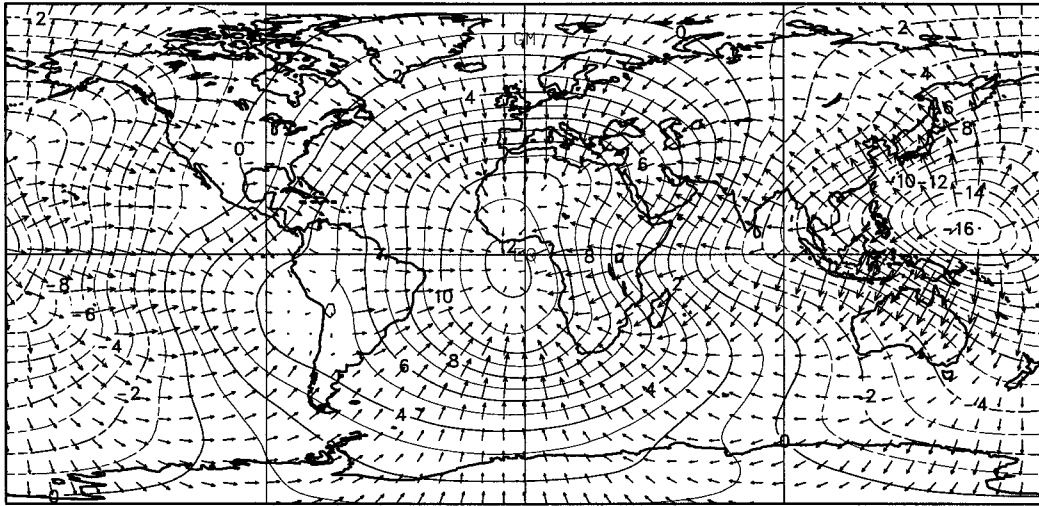
The monthly mean mixing ratio  $\chi_n$  for month  $n$  resulting from the constant, continuous source  $S$ , switched

on  $L$  months previously at the beginning of month  $n - L$ , is given by the superposition

$$\chi_n(L) = M_0 \sum_{l=0}^L G_{n,n-l}, \quad (6)$$

where  $M_0$  is the mass injected by  $S$  per month. If the atmosphere were stationary in time,  $G_{n,n-l}$  would de-

## $V_D$ and $\Phi$ at 200 mb



## $\delta V_D$ and $\delta\Phi$ at 200 mb

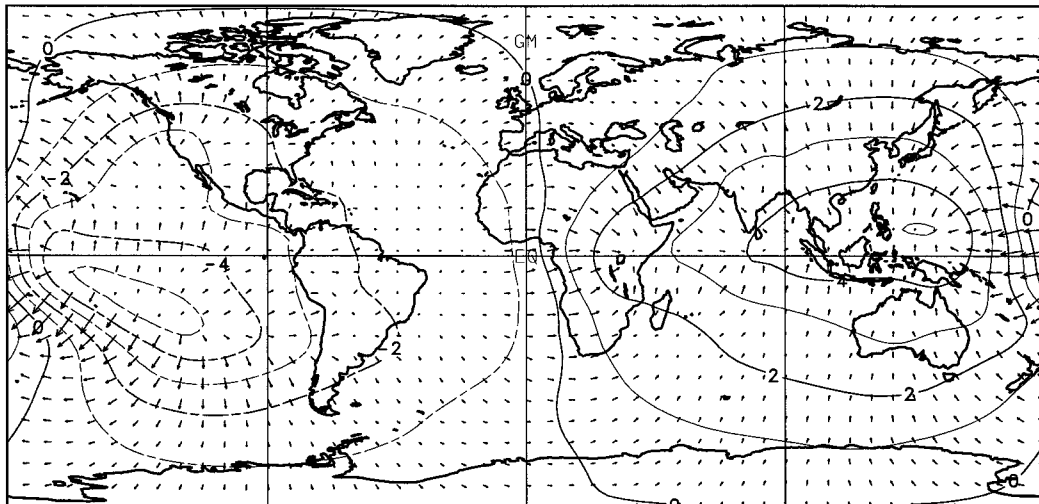


FIG. 6. (top) The 200-mb divergent wind,  $V_D = \nabla\Phi$ , and its potential function  $\Phi$ . (bottom) The change in  $\delta V_D$  and  $\delta\Phi$  under global warming. Both panels have the same scale. The contour interval for  $\Phi$  is  $10^6 \text{ m}^2 \text{ s}^{-1}$ , and the vector scale at the bottom of the lower panel indicates a velocity of  $8 \text{ m s}^{-1}$ .

pend only on the time elapsed since the source pulse occurred, that is, on the lag  $l$ . However, the atmosphere is not stationary in time, and climate is at best cyclo-stationary, so that the explicit dependence of

$G_{n,n-l}$  on both lag  $l$  and on source time,  $n - l$ , must be retained.

The study of how the evolution of  $G$  changes with climate is greatly simplified by averaging out the strong

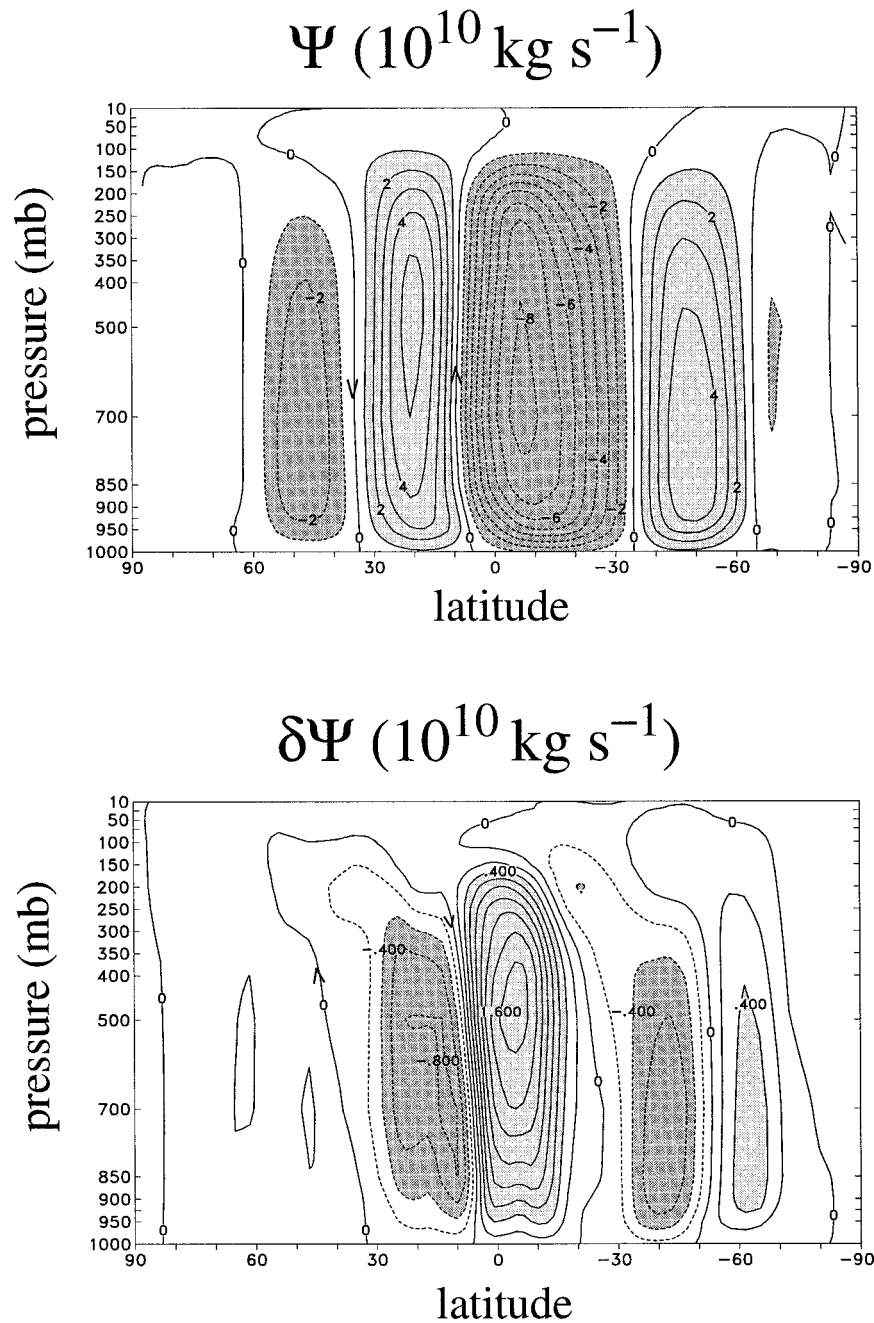


FIG. 7. The annual-mean (air) mass streamfunction  $\Psi$  and its change  $\delta\Psi$  under global warming.

seasonal dependence of  $G_{n,n-l}$  on source time,  $n - l$ . This is done by taking an annual average of the monthly means of  $G_{n,n-l}$  over  $n$  at fixed lag  $l$ . For example, for  $l = 2$  we average the March response of the January pulse, the April response of the February pulse, and so on for a complete annual cycle of 12 pulses. Thus, we define an “annual average,” or “mean” Green function,  $\bar{G}$ , through

$$\bar{G}_l \equiv \frac{1}{12} \sum_{n=n_0}^{n_0+11} G_{n,n-l}. \quad (7)$$

The average (7) formally depends also on  $n_0$ , that is, on the precise year over which this 12-month mean is computed. However, for an ensemble average over many realizations of the flow, for a climate that is approximately cyclo-stationary (in the sense that monthly sta-

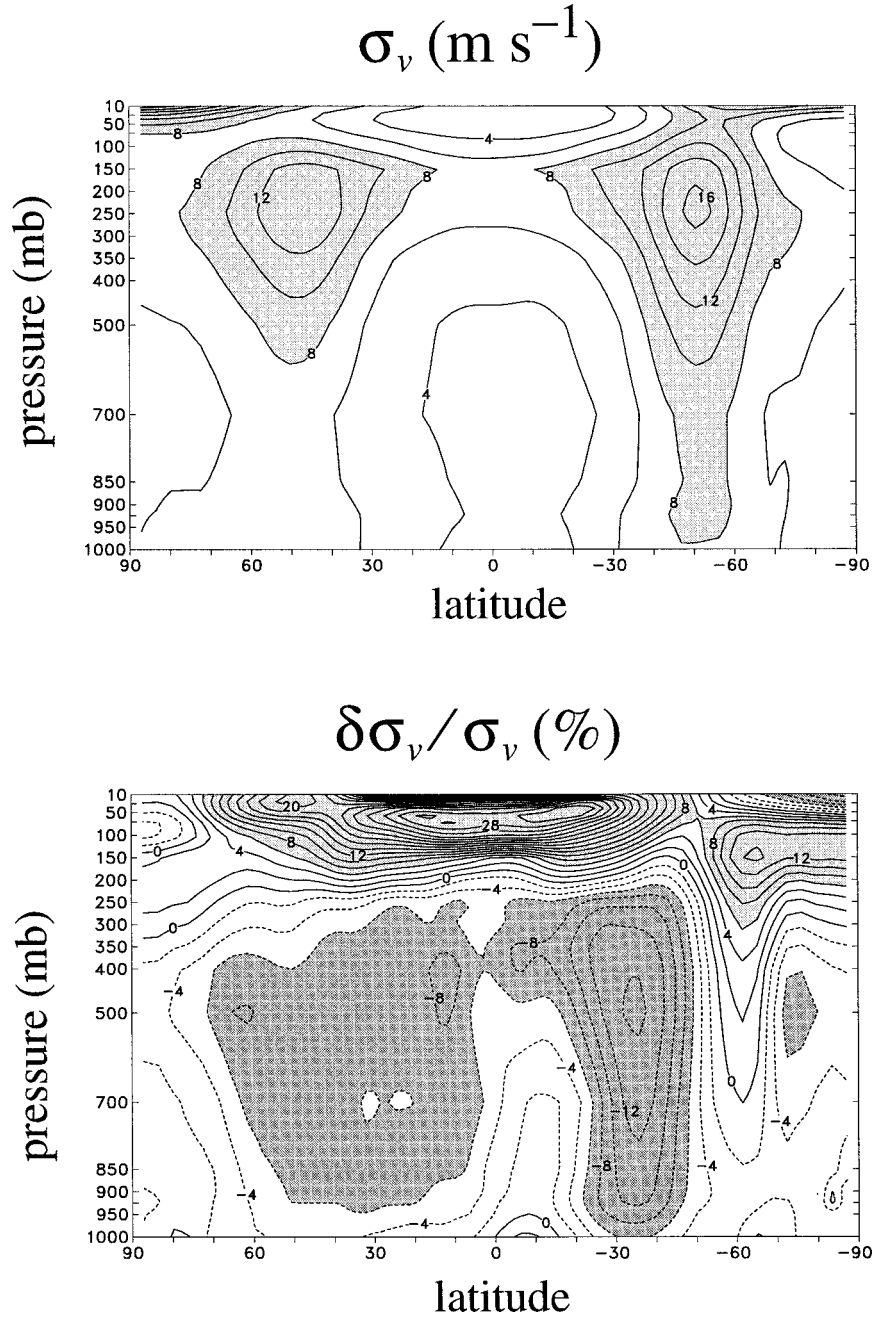


FIG. 8. (top) The std dev of the meridional wind  $\sigma_v \equiv \sqrt{[v'^2]}$  as a measure of transient eddy activity and (bottom) its percentage change.

tistics do not change from year to year), the dependence on  $n_0$  disappears. In practice, we take the average (7) over only 1 yr of simulation and assume that interannual fluctuations are weak. With increasing  $l$  this is rapidly an excellent assumption, since the ensemble fluctuations of  $G_{n,n-l}$  decay with  $l$  as  $l^{-3}$  (Holzer 1999). Even for small  $l$ , the 12-month average (7) should render interannual fluctuations small. Consequently, we neglect the dependence on  $n_0$ .

Analogous to (6), the mean Green function  $\bar{G}_l$  may be used to synthesize the annual-mean tracer mixing ratio  $\chi^+$  via the superposition

$$\bar{\chi}^+ = M_0 \sum_{l=0}^{\infty} (\bar{G}_l - G_{\infty}) + \frac{1}{2} M_0 G_{\infty}, \quad (8)$$

as discussed in the appendix. From (8), changes in  $\chi^+$  under global warming can be synthesized from the changes in  $\bar{G}$  as



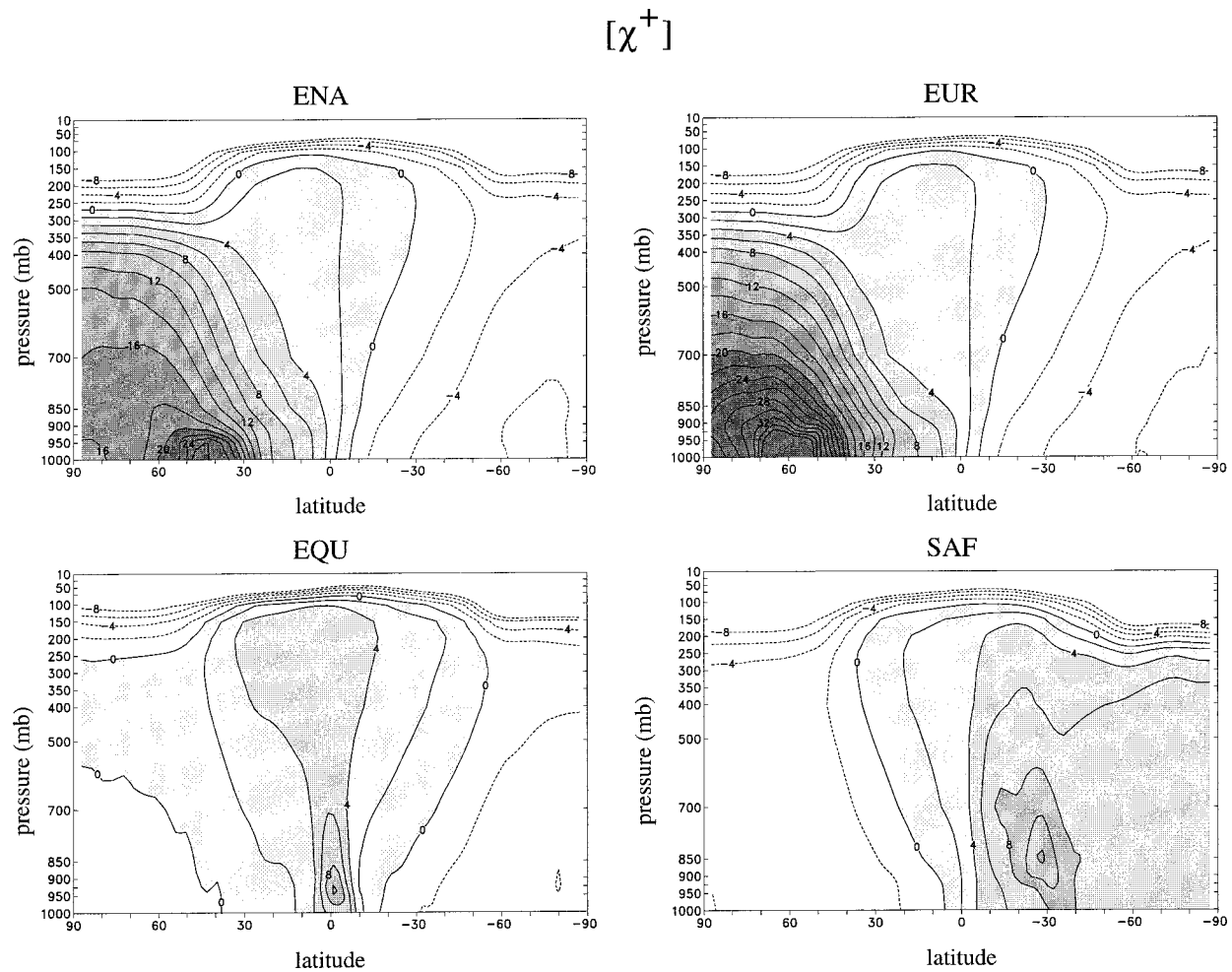


FIG. 9. (this page) The annually and zonally averaged mixing ratio  $[\chi^+]$  in the stationary state for the four sources considered. The contour interval is 2 in units of  $M_0 G_\infty$ . (following page) The corresponding change under global warming,  $\delta[\chi^+]$ . The contour interval is 0.5 in units of  $M_0 G_\infty$ .

$$\delta\overline{\chi^+} = M_0 \sum_{l=0}^{\infty} \delta\overline{G}_l. \quad (9)$$

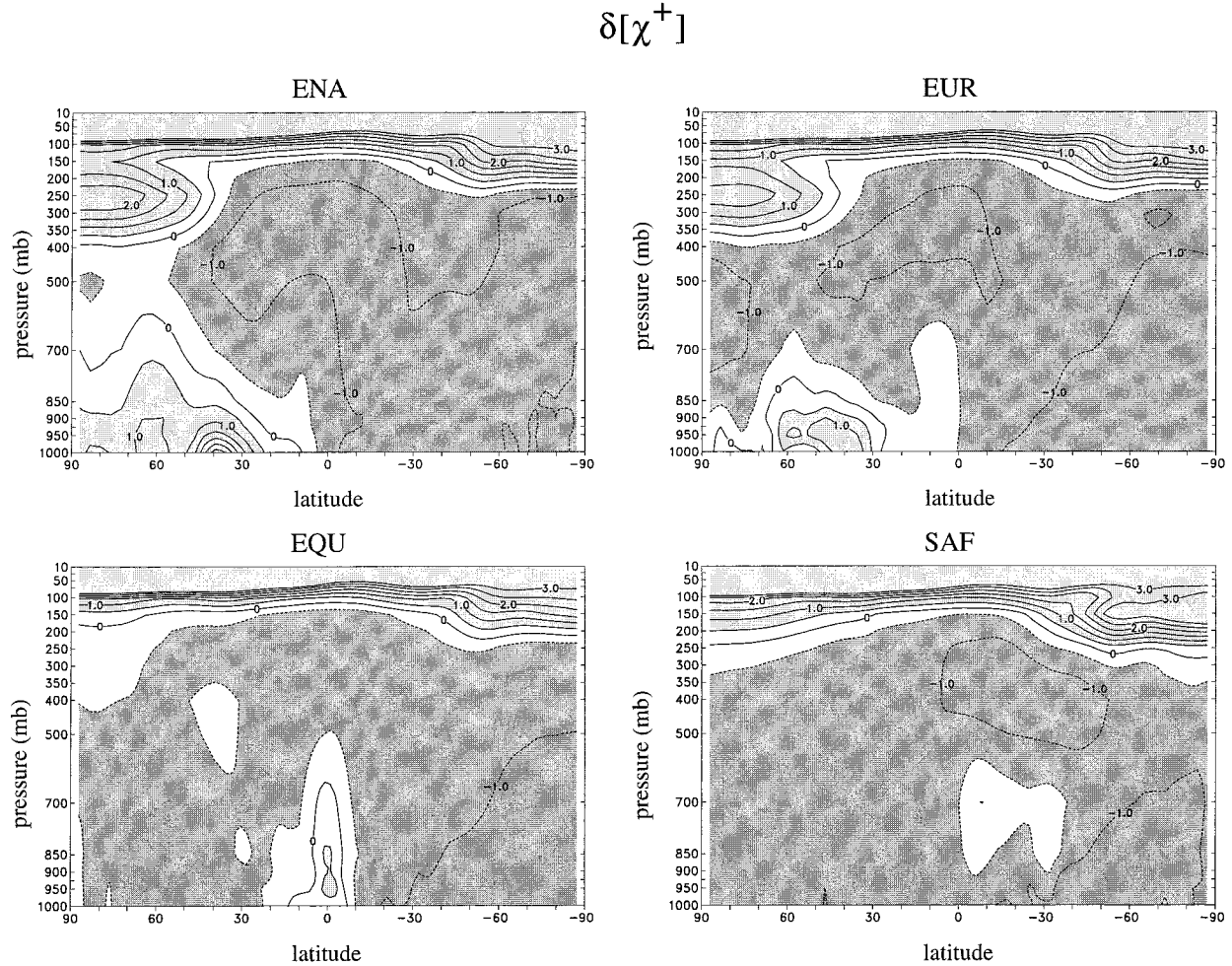
We find that in the troposphere, the rapidly convergent sum (9) is dominated by the first few most recent pulses ( $l = 0, 1$ , and  $2$ ).

The utility of  $G$ , and especially of its deseasonalized version  $\overline{G}$ , is that it allows one to study the transient evolution of mixing ratio and the associated transport pathways and mechanisms that cannot easily be extracted from the stationary state  $\chi^+$  but that contribute to  $\chi^+$  via (6) and (8). While there cannot be any climate changes in the stationary-state divergent tracer fluxes, the climate changes in the divergent fluxes of  $G$  balance changes in  $\partial_t G$  after the source pulse has ceased, and  $\partial_t G$  does not vanish on a time average since  $G$  continually evolves toward  $G_\infty$ . For the problems considered here, this is the principal advantage of casting the transport in terms of  $G$ .

### c. Transit-time distribution experiments

The third set of experiments uses time-dependent BCs on surface mixing ratio, without any explicit sources ( $S = 0$ ), in order to calculate transit-time distributions,  $g'$ . Specifying mixing ratio to be the Dirac  $\delta$ -function,  $\delta(t - t')$ , over some surface region  $\Omega$ , with zero-flux BCs elsewhere, results in a mixing ratio at a point  $\mathbf{r}$  in the atmosphere that is equal to the probability density  $g'(\mathbf{r}, \xi)$  that fluid elements traveled from  $\Omega$  to  $\mathbf{r}$  with a transit time,  $\xi = t - t'$ , between  $\xi$  and  $\xi + d\xi$  (Holzer and Hall 2000; Hall and Plumb 1994). For the large-scale transport of interest here, we take  $\Omega$  to be the polar cap north of  $45^\circ\text{N}$  and broaden the  $\delta$ -function again into a 1-month square pulse. The resulting mixing ratio gives  $g'$ , coarse grained in time, which we simulate for January and July pulses (i.e., winter and summer contact times,  $t'$ ).

The mean transit time  $\Gamma$  since a fluid element last had contact with  $\Omega$  is the first moment of  $g'$ . Calculating



an annual average of  $\Gamma$  directly from  $G'$  would require a simulation of the response to 12 surface pulses, one for each month of the year. Instead, we make use of the fact (Hall and Plumb 1994) that if the mixing ratio on  $\Omega$  is specified to increase linearly at a constant rate, that is, if  $\chi(\Omega, t) = \gamma t$ , then  $\Gamma(\mathbf{r}) = [\chi(\Omega) - \chi(\mathbf{r})]/\gamma$ , in the long time limit when  $\chi(\mathbf{r})$  increases linearly on average. In other words,  $\Gamma$  is the time for  $\chi(\mathbf{r})$  to “catch up” to  $\chi(\Omega)$ . We calculate  $\Gamma$  in this way from a simulation with  $\chi = \gamma t$  specified on the polar cap and with zero-flux BCs elsewhere. Annual averages of the resulting mixing ratio, and hence  $\Gamma$ , are then easily obtained. The mean transit time from the Northern Hemisphere polar cap to a point in the Southern Hemisphere provides a timescale for interhemispheric transport.

### 3. Changes in transport timescales

Several related transport timescales are used to characterize the change in transport climate associated with global warming. These timescales measure the rate at

which tracer mass is dispersed from the source and are, therefore, relevant for the interpretation of changes in mixing ratio.

#### a. Interhemispheric two-box time

An instantaneous “two-box” time  $\tau_h$  is commonly used to quantify interhemispheric transport (e.g., Law et al. 1996; Bowman and Cohen 1997). The timescale  $\tau_h$  is defined in terms of the interhemispheric difference in tracer mass,  $\Delta M \equiv M_N - M_S$ , and in sources,  $\Delta S \equiv S_N - S_S$ , as

$$\tau_h = 2\Delta M/\Delta S. \quad (10)$$

For the EQU source, this definition of interhemispheric exchange time cannot be used since the EQU source straddles both hemispheres with  $\Delta S = 0$ .

Figure 2 shows  $\tau_h$  for the EUR, ENA, and SAF sources for the last 5 yr of 10-yr integrations. The seasonal and interannual variability is qualitatively similar for the future and current climates. For the Northern Hemisphere EUR

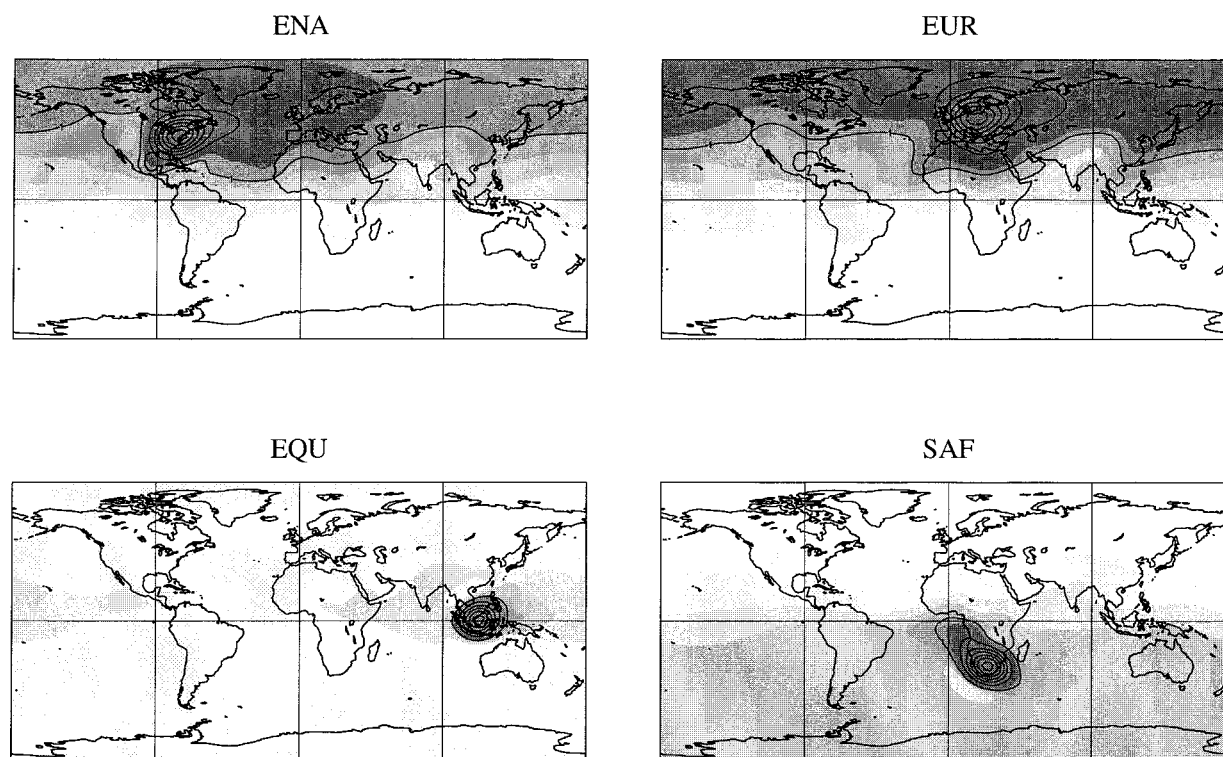
$\chi_s$ 

FIG. 10. (this page) The annually averaged surface mixing ratio  $\chi_s$  in the stationary state for the four sources considered. Contour lines have an interval of 2 in units of  $10 M_0 G_\infty$ . (following page) The corresponding change under global warming,  $\delta\chi_s$ . For plotting,  $\delta\chi_s$  has been smoothed by filtering the highest spatial wavenumbers. The contour interval is 0.4, straddling zero symmetrically, in units of  $10 M_0 G_\infty$ .

and ENA sources,  $\tau_h$  increases by about 10% from its present value. For the Southern Hemisphere SAF source, the mean change in  $\tau_h$  is small, although there is a suggestion of a change in seasonality. The fact that the Southern Hemisphere sees a weaker climate change signal than the Northern Hemisphere is consistent with the hemispheric asymmetry in the change of other variables, such as temperature (Boer et al. 2000a).

#### b. Mixing times

The time it takes for  $\bar{G}$  to first reach  $G_\infty/2$  defines a timescale,  $\tau_{1/2}$ , at every point of the atmosphere (Holzer 1999). At tropospheric locations remote from a midlatitude source,  $\tau_{1/2}$  characterizes the rate at which tracer is mixed throughout the troposphere. In practice we determine  $\tau_{1/2}$  from  $\bar{G}$  linearly interpolated in time.

Figure 3 (upper panel) shows the zonal and annual average of  $\tau_{1/2}$  for the ENA source. Only 24 months of evolution were used to obtain  $\tau_{1/2}$  and regions of the stratosphere that did not reach  $G_\infty/2$  within 24 months have been masked out. The timescale  $\tau_{1/2}$  increases with distance from the source and, in the Southern Hemisphere, attains values of about 0.5 yr, on the order of the interhemispheric exchange time  $\tau_h$ . The EUR source gives a similar pattern of  $\tau_{1/2}$  (not shown), while

the EQU and SAF sources (also not shown) have maximum tropospheric  $\tau_{1/2}$  values in the Southern and Northern Hemisphere, respectively ( $\sim 0.4$  yr for EQU and  $\sim 0.2$  yr for SAF). The changes  $\delta\tau_{1/2}$  are about 10% for all sources. As can be seen from Fig. 3 (lower panel), in the changed climate it would take a long-lived pollutant released in the Northern Hemisphere about 2.5 weeks longer to exceed a monthly mean threshold concentration in the Southern Hemisphere than it does now. (The large reductions in  $\tau_{1/2}$  in the lower northern stratosphere are due to a slight upward shift in the tropopause as discussed below.) Longer mixing times in the changed climate also imply larger pollutant concentrations near the source, since the flow is slower in dispersing tracer.

#### c. Transit-time distribution

Figure 4 shows the probability density functions (pdfs)  $G'(\xi)$  of transit times  $\xi$  since air parcels at the equator and South Pole last had contact with the 45°N polar cap during January, for the current and future climates. The pdfs shown are for the surface, and the equator pdf has been zonally averaged. The response to a July pulse (not shown) is qualitatively similar, although close to the polar cap,  $G'$  is peaked at shorter



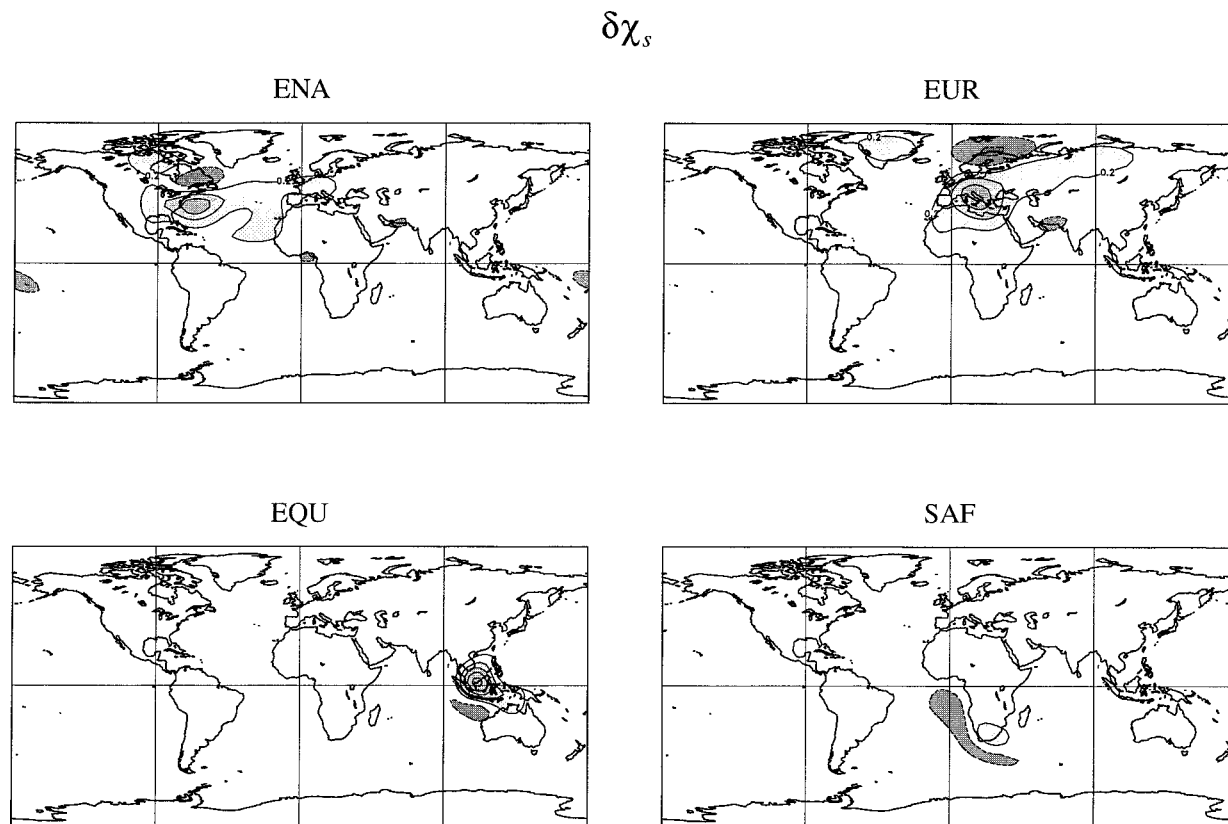


FIG. 10. (Continued)

times, indicating more rapid summertime interhemispheric transit, presumably because of the northward excursion of the ITCZ. There are no dramatic changes in the structure of the pdfs with climate change, but in the perturbed climate their peaks occur at slightly longer times and their exponential tails decay more slowly. A least squares fit to  $g'(\xi) \sim \exp(-\xi/\tau)$  for the tails gives a decay time of  $\tau \sim 2.6$  yr for the current climate, and of  $\tau \sim 2.8$  yr for the future climate. On a zonal average (not shown),  $\tau$  and its change  $\delta\tau$  have little structure throughout the troposphere. For stationary transport, the exponential tail of  $g'$  is associated with the most slowly decaying mode of the transport operator, which is consistent with the spatial uniformity of its corresponding eigenvalue,  $1/\tau$  (see, e.g., Hall et al. 1999).

The mean transit time,  $\Gamma \equiv \int_0^\infty \xi g'(\xi) d\xi$ , is sensitive to the tails of the pdf. Figure 5 shows that in the zonal and annual mean,  $\Gamma$  increases by about 10% in the warmer climate. We cannot draw conclusions about  $\delta\Gamma$  in the stratosphere, because the 10-yr simulation is too short for the surface BC to fully propagate throughout the stratosphere.

#### 4. Climate changes in spatial structure

Section 3 shows that interhemispheric exchange, mixing, and transit times all increase, implying less active

transport in the warmer climate. Here we investigate changes in the spatial structure of some basic circulation features, followed by a more extensive examination of changes in tracer mixing ratio.

##### a. Changes in circulation features

Most GCM studies of climate change concentrate on changes in temperature and hydrological/cryospheric quantities such as precipitation, snow and ice, and soil moisture. Dynamical aspects of climate change receive less attention. On the synoptic scale, simulated dynamical changes include those in the intensity and distribution of extratropical cyclones (e.g., Hall et al. 1994; Lambert 1995; Carnell and Senior 1998; S. J. Lambert 2000, personal communication). A number of authors investigate changes in large-scale transports (e.g., Branscome and Gutowski 1992; Coleman et al. 1994; Boer 1995; Carnell and Senior 1998). They find a general decrease in the poleward transport of momentum and of internal-plus-potential energy, which, depending on the model, is partially or completely offset by an increase in latent energy transport. The rate of working of the atmosphere, as measured by the generation of available potential energy, its conversion to kinetic energy and subsequent dissipation, decreases overall by



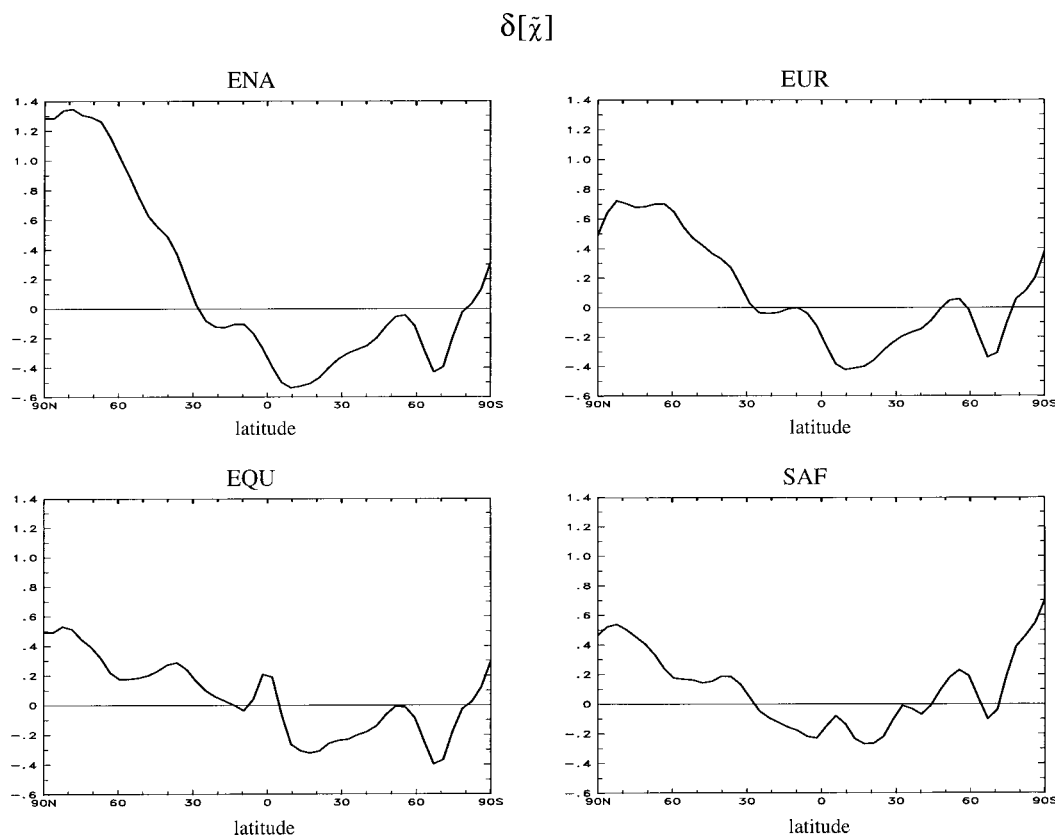


FIG. 11. The annually and zonally averaged change in the tracer burden  $\delta[\tilde{\chi}]$ , in units of  $M_0\langle\tilde{G}_x\rangle$ , for the four sources considered.

about 10% in a  $2 \times \text{CO}_2$  climate change simulation (Boer 1995).

Changes in the divergent mean flow will affect tracer transport. Figure 6 shows the annual average of the divergent flow component,  $\overline{\mathbf{V}}_D$ , at 200 mb in the upper troposphere. This divergent flow constitutes the upper branches of the north–south Hadley and east–west Walker circulations in the Tropics, which are broadly matched by a reversed pattern in the lower troposphere. There is a weakening of the divergent flow (as well as some shifts of pattern) in the warmer climate (Fig. 6, lower panel). The pattern of the change in the divergent flow resembles that associated with ENSO. In the warmer climate, relatively warmer SSTs in the central and eastern tropical Pacific and relatively cooler SSTs in the western Pacific lead to ENSO-like climate changes in the precipitation patterns (Boer et al. 2000a). This is a common result of climate change simulations (e.g., Meehl et al. 2000). The associated meridional circulation and its change are shown in Fig. 7 in terms of the annual-mean mass streamfunction  $\Psi$ . The strength of the Hadley circulation, as measured by  $\Psi$ , is reduced by about 10%.

The temporal standard deviation of the meridional velocity gives a measure of the vigor of the transient eddies that are also important in transport. The upper panel of Fig. 8 shows  $\sigma_v \equiv \sqrt{[v'^2]}$ . Both  $\sigma_v$  and the

corresponding  $\sigma_u$  (zonal winds) have similar magnitudes. The lower panel displays  $\delta\sigma_v/\sigma_v$ , showing that the transient eddies decrease throughout much of the troposphere. The pattern of the eddy variance in the warmer climate (not shown) is very similar to that of the current climate with nearly identical peak values, but with a slight overall upward shift of the pattern. For both mean and transient flow components, the overall picture is of modestly less active large-scale flow dynamics in the warmer climate. The changes in circulation discussed here should be robust in that current climate models respond in broadly similar ways to changes in greenhouse-gas-plus-aerosol forcing (e.g., Cubash et al. 2001).

#### b. Changes in tracer distribution

Figure 9 shows the stationary-state annually and zonally averaged mixing ratios  $[\chi^+]$  for each of the four sources for the current climate, together with the changes  $\delta[\chi^+]$  under global warming. The dominant features of  $\delta[\chi^+]$  are a pronounced increase in the stratosphere and a corresponding overall broad reduction in the troposphere, but with locally enhanced mixing ratio close to the sources. Figure 10 shows the lowest-model-level mixing ratio  $\chi_s$  and its change  $\delta\chi_s$ . A “plume” of enhanced concentration

extends downwind from the source. The enhancement is common to all source cases with  $\delta\chi_s^+/\chi_s^+$  on the order of 10% in the plume. The enhancement is most pronounced for the Northern Hemisphere sources and least pronounced for the SAF source. The changes  $\delta[\bar{\chi}]$  in the annually and zonally averaged tracer burdens (Fig. 11) show that for the EUR and ENA sources, tracer mass is redistributed to the Northern Hemisphere. The mass redistribution for the EQU and SAF sources is more subtle, with smaller increases in Northern Hemisphere mass. The equatorial enhancement for the EQU source comes from a highly localized peak in the tracer burden change centered on the source (not shown).

### 1) TWO-BOX MODEL FOR STRATOSPHERIC ENHANCEMENT

The enhanced mixing ratios in the stratosphere and the corresponding overall depressed tropospheric mixing ratios of the future climate can be attributed to an upward shift in the tropopause. While the GCM cannot give a realistic representation of the stratosphere with 10 vertical levels, the model nevertheless produces a tropopause that acts as a transport barrier. Here we investigate the effects of changes in tropopause level and in stratosphere–troposphere exchange (“strat–trop exchange,” for short) on mixing ratio using a simple two-box model.

The troposphere is represented by a box of air with mass  $\alpha M_A$  and the stratosphere is represented by a box of mass  $(1 - \alpha)M_A$ , where  $\alpha$  is the fractional mass of the troposphere. The two boxes are assumed to be sufficiently well mixed, with mixing ratios  $\chi_l$  (lower box, troposphere) and  $\chi_u$  (upper box, stratosphere), so that the cross-tropopause flux is reasonably represented as being proportional to  $\chi_l - \chi_u$ . With tracer masses  $M_l$  and  $M_u$  and a tropospheric source of tracer mass,  $S$ , the two-box model is then given by

$$\begin{aligned} \partial_t M_l &= -K(\chi_l - \chi_u) + S \\ \partial_t M_u &= -K(\chi_u - \chi_l), \end{aligned} \quad (11)$$

where we take  $K$  and  $\alpha$  as constant but not necessarily the same for the current and future climates. Expressing the tracer masses in terms of mixing ratios, that is,  $M_l = \alpha M_A \chi_l$  and  $M_u = (1 - \alpha)M_A \chi_u$ , (11) is easily solved for  $\chi_l$  and  $\chi_u$ . The steady-state values of  $\chi_l^+ = \chi_l - \chi^0$  and  $\chi_u^+ = \chi_u - \chi^0$  are given by

$$\chi_l^+ = s\tau(1 - \alpha)^2, \quad \chi_u^+ = -s\tau\alpha(1 - \alpha), \quad (12)$$

where  $\tau \equiv M_A/K$  is an effective strat–trop exchange time,  $s \equiv S/M_A$ , and  $\chi^0 = (M_l + M_u)/M_A$ . Note that  $\chi_u^+ < 0$  (stratosphere) and  $\chi_l^+ > 0$  (troposphere), consistent with the four left panels of Fig. 9.

In the context of this two-parameter box model, a change in climate is represented by a change in exchange time  $\delta\tau$  and/or in the position of the tropopause represented here by  $\delta\alpha$ . From (12), the corresponding

induced fractional changes in stationary-state mixing ratio are to first order

$$\begin{aligned} \frac{\delta\chi_l^+}{|\chi_l^+|} &= \frac{\delta\tau}{\tau} - \left( \frac{2\alpha}{1 - \alpha} \right) \frac{\delta\alpha}{\alpha} \\ \frac{\delta\chi_u^+}{|\chi_u^+|} &= -\frac{\delta\tau}{\tau} + \left( \frac{2\alpha - 1}{1 - \alpha} \right) \frac{\delta\alpha}{\alpha}. \end{aligned} \quad (13)$$

For fixed  $\tau$ , (13) shows that an increase in tropopause height ( $\delta\alpha > 0$ ) results in an overall decrease in the positive value of  $\chi_l^+$  of the troposphere and an increase (since  $2\alpha - 1 > 0$ ) in the negative value of  $\chi_u^+$  in the stratosphere. This simply reflects that, in the changed climate, the same constant source is trying to fill up a larger troposphere (smaller stratosphere), so that, at any given time, the average tropospheric (stratospheric) mixing ratio is smaller (larger) than for the current climate. The four right panels of Fig. 9 show just such an average decrease in  $\chi^+$  for the troposphere (despite the local increase near the source) and corresponding increase for the stratosphere. Mixing ratios can also change if  $\tau$  changes. From (13), an increased  $\tau$  (less vigorous strat–trop exchange) leads to increased tropospheric and decreased stratospheric mixing ratios, as expected.

We analyze the constant-tracer-source simulations in the context of this two-box model. A climatological tropopause is defined for this purpose as the locus of the highest pressures (lowest heights), where the vertical gradient of the mean annual temperature,  $\partial\bar{T}/\partial p$ , exceeds  $10^{-3} \text{ K Pa}^{-1}$ . This gives the fractional mass of the troposphere as  $\alpha = 0.853$  for the current climate with a climate change of  $\delta\alpha/\alpha = +2.22\%$ . With the tropopause located, the mass-averaged mixing ratios  $\chi_l^+$  and  $\chi_u^+$  can be calculated from the annually averaged simulation data, so that by using (12) all the terms of (13) may be determined. Table 1 gives the values for the EUR case; the results for the other sources are very similar. Given the overall reduction in the vigor of the large-scale circulation, it is perhaps surprising that strat–trop exchange is *enhanced* in this model for the future climate, with  $\delta\tau/\tau = -6.16\%$ . However, given the poor representation of the stratosphere we do not attach much significance to the values of  $\tau = 12 \text{ yr}$  and  $\delta\tau = -0.7 \text{ yr}$ .

The decrease of  $\tau$  and the increase of  $\alpha$  both act to increase the mixing ratio of the stratosphere and to decrease that of the troposphere. The dominant terms of (13) come from the change of the tropospheric mass,  $\delta\alpha/\alpha$ . Although the tropospheric air mass only increases by  $\sim 2\%$ , the corresponding change in  $\chi_l^+$  is a substantial decrease by  $\sim 26\%$ . Note that the small  $\delta\alpha/\alpha$  is amplified by its prefactors  $\propto 1/(1 - \alpha)$  in (13). Of course, with a constant source,  $\chi^0$  grows as  $st$  and  $\delta\chi/\chi \approx \delta\chi^+/\chi^0 \rightarrow 0$  as  $t \rightarrow \infty$ . The large changes  $\delta\chi^+/\chi^+$  represent large changes in the spatial *structure* superposed on the uniform, growing background  $\chi^0$  and not a significant change in absolute concentration. Here, an increase in tropopause height results in reduced cross-tropopause tracer gradients.

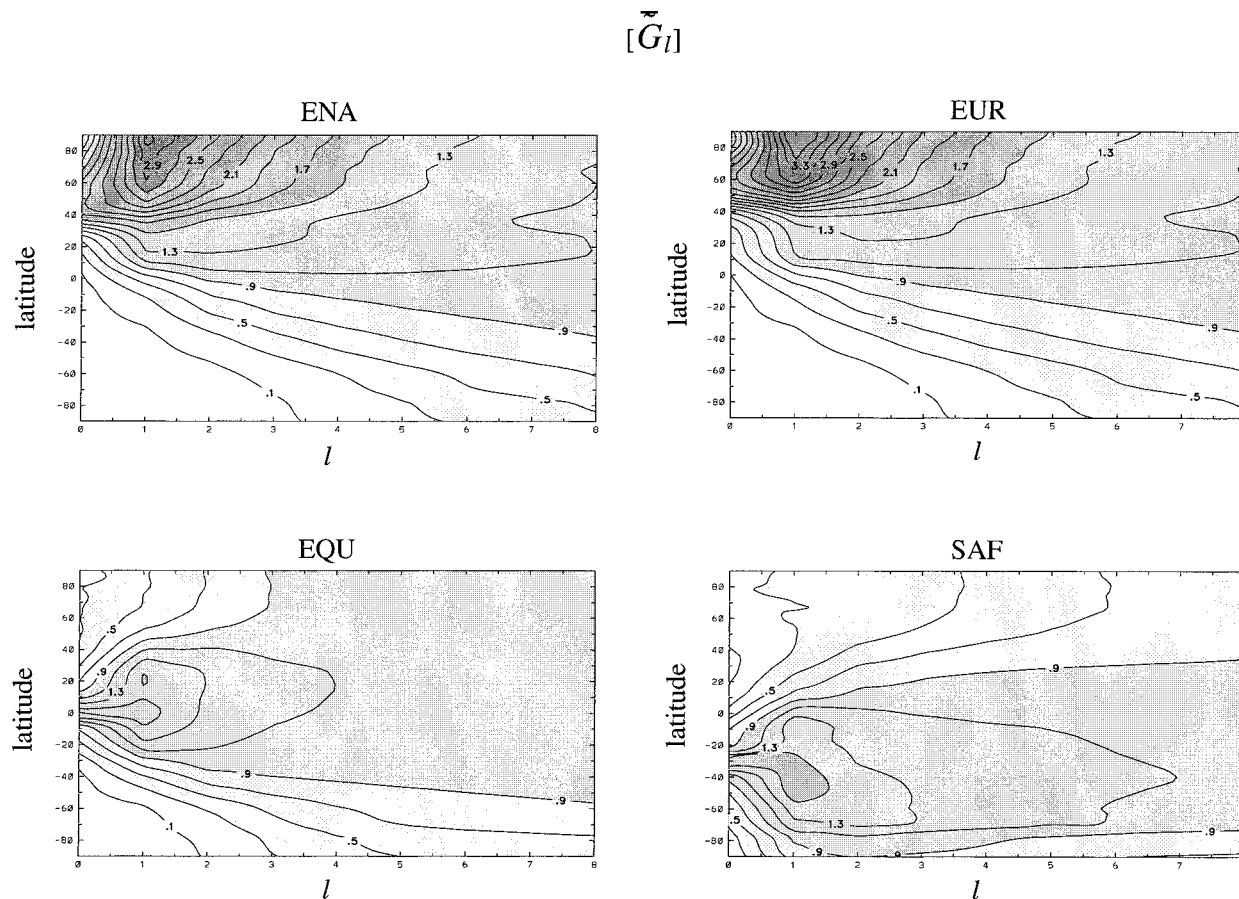


FIG. 12. (this page) The evolution of the zonally averaged burden  $[\bar{G}_l]$  with time since tracer release (lag time)  $l$ , in months, for the four sources considered. The contour interval is 0.2 in units of  $\langle \bar{G}_\infty \rangle$ . (following page) The corresponding change  $\delta[\bar{G}_l]$ . The contour interval is 0.2, straddling zero symmetrically, in units of  $0.1 \langle \bar{G}_\infty \rangle$ .

## 2) TRACER MASS REDISTRIBUTION

For the statistically stationary  $\chi^+$ , a change in transport climate implies the redistribution of tracer mass seen in Figs. 9–11. Here we ask if we can identify a mechanism for this redistribution. A reduced Hadley circulation, weaker eddy variance, and slower transit times in the future climate all imply higher tracer mass burdens in the source hemisphere. The enhanced mixing ratio close to the source follows since slower transport should lead to relatively more tracer being “left behind.” However, in the stationary state with a constant source, the time-averaged divergent tracer flux must be the same for both the present and future climates as pointed out in section 2a. Changes in the nondivergent stationary-state tracer fluxes themselves are not easily interpreted in terms of changes in mixing ratio. Zonal averages of these changes in tracer fluxes are purely rotational in the  $p$ -latitude plane, like the atmospheric mass fluxes themselves. Similar arguments apply to the changes in the traditional eddy components of the tracer fluxes. While the mean and eddy components of the flux (not shown) change with climate, the net transport can-

not change. The largest changes occur for the mean-motion flux and are compensated by changes in the eddy fluxes, whose patterns are not readily interpreted in terms of changes in mixing ratio.

The Green function allows the stationary state with constant sources to be analyzed from a different perspective, since that state can be synthesized from  $G$  as in (6) or (8). Thus, the evolution of  $G$  gives information on how the equilibrium state is maintained from the continual superposition of time-lagged  $G$ s. To avoid the complexities of the seasonal dependence of  $G$  on source time, we consider here only  $\bar{G}_l$ , the average of  $G$  at fixed lag, which depends only on the number of months elapsed,  $l$ , since the source pulse occurred [cf. (7)].

Figure 12 shows the zonally averaged vertically integrated burden,  $[\bar{G}_l] \equiv [\int_0^{p_0} dp \bar{G}_l / g]$  as a function of lag  $l$ , together with its change  $\delta[\bar{G}_l]$ . Since  $\bar{G}$  eventually approaches  $G_\infty$  in both the current and changed climates, the difference  $\delta[\bar{G}_l]$  vanishes with increasing  $l$ . The change in the evolution toward  $G_\infty$  (Fig. 12, right four panels) shows that in the future more tracer mass from the ENA and EUR sources is retained in the Northern

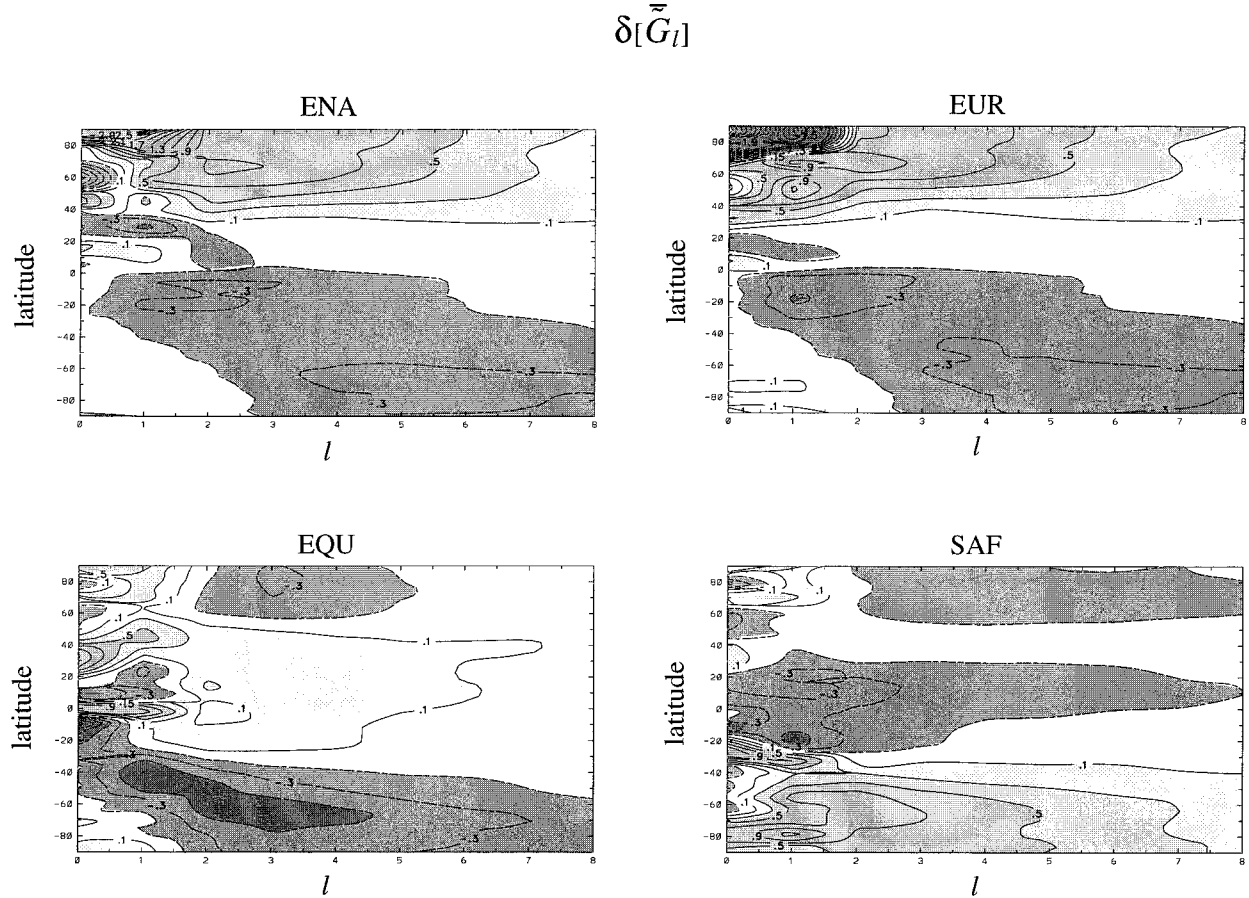


FIG. 12. (Continued)

Hemisphere, consistent with a weakened interhemispheric exchange. For the EQU case, the mass injected at the equator is preferentially dispersed to the Northern Hemisphere (Fig. 12, left four panels) and this hemispheric asymmetry becomes more pronounced in the changed climate (Fig. 12, right four panels). The climate change for the SAF source shows an increased retention southward of the source in the Southern Hemisphere, again consistent with decreased interhemispheric exchange. Note that the SAF source also produces decreased burdens north of the source in the Southern Hemisphere, consistent with the weak climate change signal in  $\tau_h$  (section 3a), which implies a small change in the hemispherically integrated masses. In all cases, the redistribution of  $[\bar{G}_l]$  peaks for  $l \sim 1$ .

For small lag  $l$  (few months after the source month), the resolved monthly mean flux,  $(\bar{v}G_l, \bar{\omega}G_l)$ , is largely divergent and gives an indication of the transport pathways taken by the tracer. An examination of the evolution of  $G$  for the current climate (Holzer 1999) showed that transport in the CCCma model is consistent with the picture of Plumb and Mahlman (1987) and Plumb and McConalogue (1988): tracer from midlatitude surface sources is drawn into the ITCZ, injected into the

upper troposphere, and then enters the opposite hemisphere aloft in the outflow region of the ITCZ. This “tracer fountain” can be seen in the zonally averaged flux  $([\bar{v}G_l], [\bar{\omega}G_l])$  of Fig. 13 together with the changes  $([\delta\bar{v}G_l], [\delta\bar{\omega}G_l])$  ( $l = 1$  corresponds to the month following the source month). The climate changes in the flux show a suppression of the tracer fountain, with corresponding circulations on either side of the annual-mean ITCZ. The reduced fountain represents a large-scale mechanism for the suppression of interhemispheric exchange in the future climate. The tracer fountain and its climate change are particularly clearly evident for the EQU source. The heart of the divergent winds, which is a “fountain of air” (Fig. 6), lies about  $\sim 50^\circ$  east of the EQU tracer fountain (as located in a longitudinal section, not shown). The suppression of the tracer fountain is consistent with a change in the global flow pattern involving the Hadley–Walker circulation, discussed in section 4a (Figs. 6 and 7).

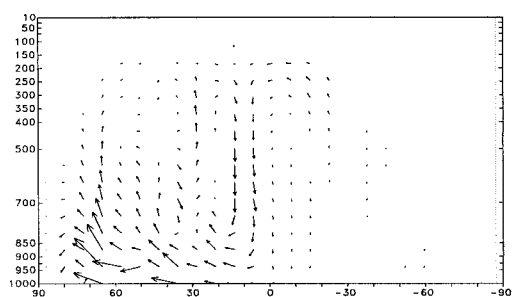
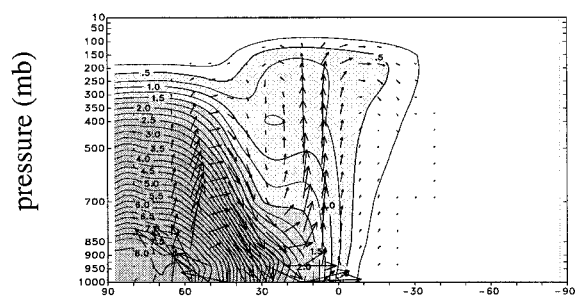
### 3) ENHANCED NEAR-SOURCE MIXING RATIO

The enhanced tracer mixing ratio close to the sources is examined here in terms of changes in the evolution

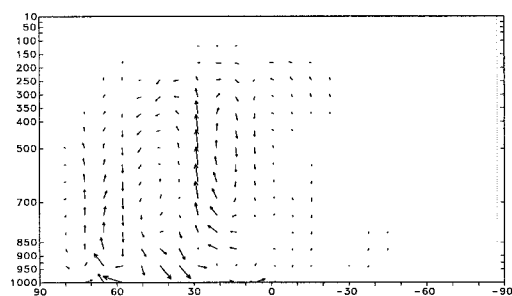
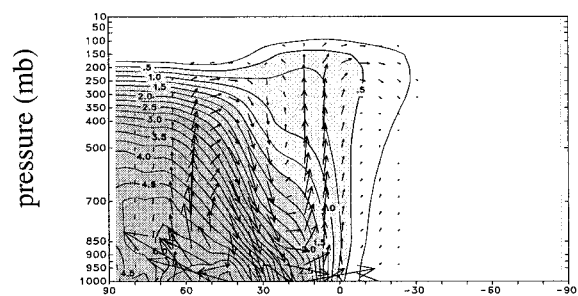


$\cos\phi([\overline{vG_1}], [\overline{\omega G_1}]) \text{ and } [\overline{G_1}]$ 
 $2 \times \cos\phi(\delta[\overline{vG_1}], \delta[\overline{\omega G_1}])$ 

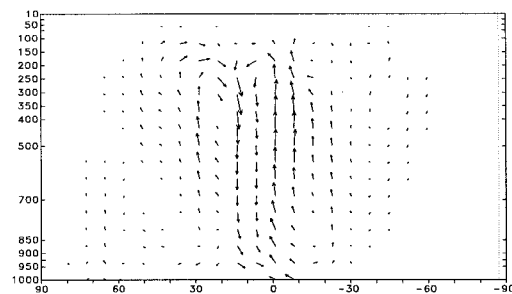
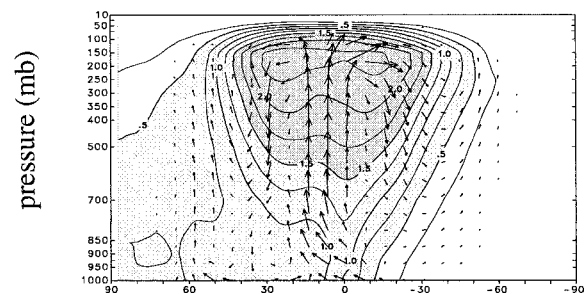
EUR



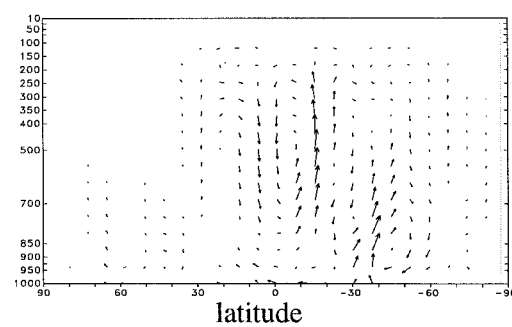
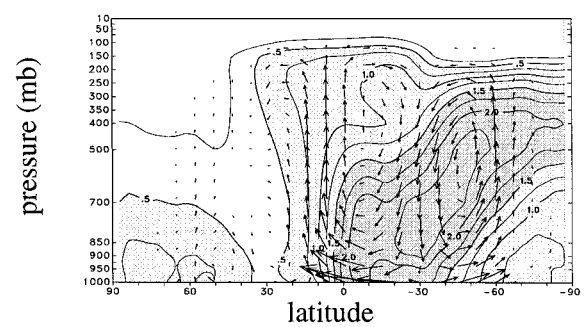
ENA



EQU



SAF



of the mean Green function  $\overline{G}_l$  under global warming. Figure 14 shows the evolution of the global horizontal average,  $\langle \overline{G}_l \rangle$ , and its change,  $\delta \langle \overline{G}_l \rangle$ , as a function of pressure and elapsed number of months  $l$ . The largest values of  $\langle \overline{G}_l \rangle$  occur at low levels for the ENA, EUR, and SAF sources, but for the EQU source, the “fountain” and tropical convection lift the maximum of  $\langle \overline{G}_l \rangle$  to the upper troposphere. For all sources, the changes  $\delta \langle \overline{G}_l \rangle$  exhibit enhanced values at low levels for the first one or two months, and at stratospheric levels for all lags  $l$ . After about 4 months, the mixing ratio is reduced throughout the troposphere, consistent with the results of the two-box model [section 4b(1)]. The evolution of  $\delta \langle \overline{G}_l \rangle$  shows that the enhanced near-surface mixing ratio of the stationary state in the warmer climate comes from the relative accumulation of tracer during the first few months after its injection. The evolution of the vertical profile of  $\delta \overline{G}_l$  at the source (not shown) leads to the same qualitative picture.

We now seek to identify the near-surface accumulation of  $\delta \overline{G}_l$  with changes in specific processes represented by separate terms in the equation of motion for  $\overline{G}_l$ . We write (5) for  $G$ , averaged over months and then annually at fixed lag  $l$ , as

$$\partial_t \overline{G}_l = S_\delta \Delta_{l,0} + \overline{\mathcal{A}(G)}_l + \overline{\mathcal{D}(G)}_l, \quad (14)$$

where  $\mathcal{A}(X) = -\nabla \cdot (\mathbf{v}X) - \partial_p(\omega X)$  denotes the rate of change, or “tendency,” of  $X$  due to resolved advection, and  $\Delta_{l,0}$  is the fixed-lag “average” of the square pulse of (5), so that  $\Delta_{l,0}$  is nonzero only if  $l = 0$ , with  $\Delta_{0,0} = 1 \text{ month}^{-1}$ .

Figure 15 shows vertical profiles of the changes  $\delta \overline{\mathcal{A}}_l$  and  $\delta \overline{\mathcal{D}}_l$  at the source locations for  $l = 0$  (the average over the months during which the source is on). Global horizontal averages of these tendencies do not give a clear picture of the dynamics in the source area, because opposing tendencies at the source, and over regions remote from the source, are averaged together. For all source cases  $\delta(\overline{\mathcal{A}} + \overline{\mathcal{D}})$  shows a net tendency to accumulate  $\delta \overline{G}$  at low levels during the source month. For subsequent months (not shown) this accumulation tendency diminishes rapidly with increasing  $l$ . Changes in the advection and subgrid terms are of the same order of magnitude, but do not have the same sign for all sources. While for the EUR and EQU cases advection and subgrid terms cooperate in accumulating low-level tracer, for the SAF case low-level accumulation is due to changes in the subgrid terms that win over opposing changes in low-level resolved tracer-flux divergence. For the EUR source, most of the accumulation occurs for lag times less than one month, which is not

captured by the 12-month average of monthly means at fixed lag shown. Nevertheless, the EUR case suggests that, at the EUR location, low-level accumulation is dominated by flux convergence and opposed by the subgrid terms, opposite to the situation for SAF. For ENA,  $\delta \overline{\mathcal{A}}$  appears to play a minor role in controlling the low-level accumulation of  $\delta \overline{G}$ .

## 5. Variance budget of the stationary state

Although the Green function formally contains complete information on tracer transport and distribution, changes are nevertheless difficult to characterize in terms of a simple mechanistic picture even with that approach. Here we adopt a traditional budget approach applied to tracer variance in order to obtain another characterization of changes in transport climate.

For constant sources, changes in the time-averaged terms of the tracer (2) are highly constrained and not very revealing as noted in section 2a. Some information may, however, be gained from the stationary-state variance budget using variance as a measure of the spatial and temporal structure of the tracer. The standard decomposition of the variance into its mean and transient eddy terms under suitable averaging (denoted here by an overbar) is  $\overline{\chi^2} = \overline{\chi^2} + \overline{\chi'^2}$ , where we now write  $\chi$  instead of  $\chi^+$  to simplify notation. The equations for the mean and transient variances,  $\overline{\chi^2}$  and  $\overline{\chi'^2}$ , follow from (2) and, when integrated globally over the mass of the atmosphere, give the budget equations

$$\partial_t A_{\mathcal{M}} = -C + H_{\mathcal{M}} - D_{\mathcal{M}}, \quad \partial_t A_{\mathcal{T}} = C - D_{\mathcal{T}}, \quad (15)$$

where

$$A_{\mathcal{M}} \equiv \frac{1}{2} \int \overline{\chi^2} dM \quad \text{and} \quad A_{\mathcal{T}} \equiv \frac{1}{2} \int \overline{\chi'^2} dM, \quad (16)$$

$$C \equiv - \int (\overline{\chi' \nabla' \cdot \nabla \chi} + \overline{\chi' \omega' \partial_p \chi}) dM, \quad (17)$$

$$H_{\mathcal{M}} \equiv 4\pi a^2 \langle \phi \overline{\chi_s} \rangle, \quad (18)$$

$$D_{\mathcal{M}} \equiv -g \int \overline{f \partial_p \chi} dM, \quad \text{and}$$

$$D_{\mathcal{T}} \equiv -g \int \overline{f' \partial_p \chi'} dM. \quad (19)$$

As indicated in the upper panel of Fig. 16, mean tracer variance  $A_{\mathcal{M}}$  is generated at rate  $H_{\mathcal{M}}$  by the constant

←

FIG. 13. The annually and zonally averaged resolved fluxes ( $[\overline{vG}_1]$ ,  $[\overline{\omega G}_1]$ ) for the current climate (left column) and their changes ( $[\delta \overline{vG}_1]$ ,  $[\delta \overline{\omega G}_1]$ ) (right column). [Horizontal fluxes are multiplied by cosine of latitude ( $\cos \phi$ ) so that they are proportional to the meridional mass flux. Vertical fluxes are scaled so that the direction of the vectors is meaningful on the figure.] For the current climate, the fluxes are superposed on  $[\overline{G}_1]$ , with a contour interval of 0.25 in units of  $G_\infty$ . The vector scale at the bottom of the figure indicates a horizontal flux of  $5G_\infty \text{ m s}^{-1}$  for the current climate and  $2.5G_\infty \text{ m s}^{-1}$  for the change.

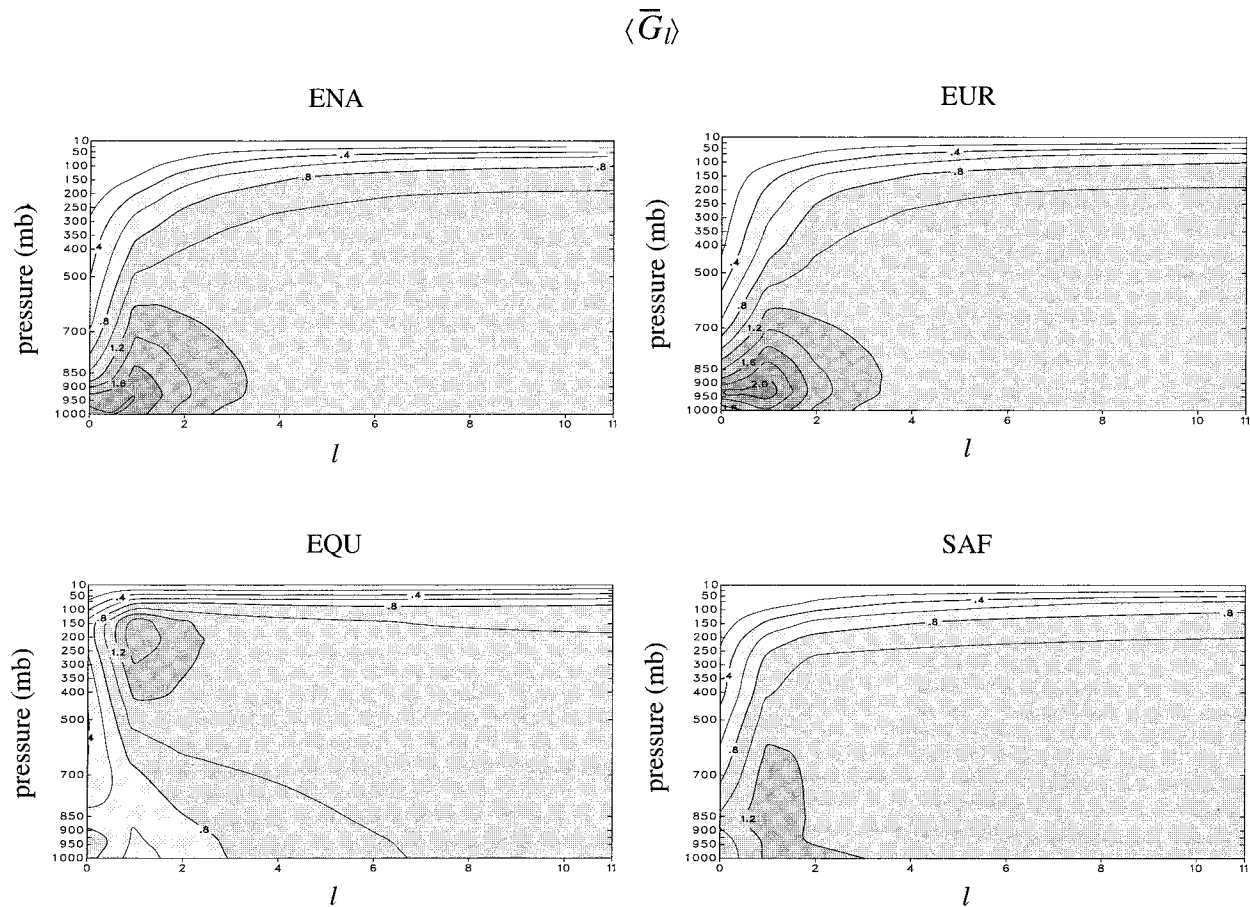


FIG. 14. (this page) Evolution of the horizontally averaged Green function,  $\langle \bar{G}_l \rangle$ , with time since release (lag time)  $l$ , in months, for the four sources considered. The contour interval is 0.2 in units of  $G_\infty$ . (following page) The corresponding change  $\delta \langle \bar{G}_l \rangle$ . The contour interval is 0.2, straddling zero symmetrically, in units of  $0.1 G_\infty$ .

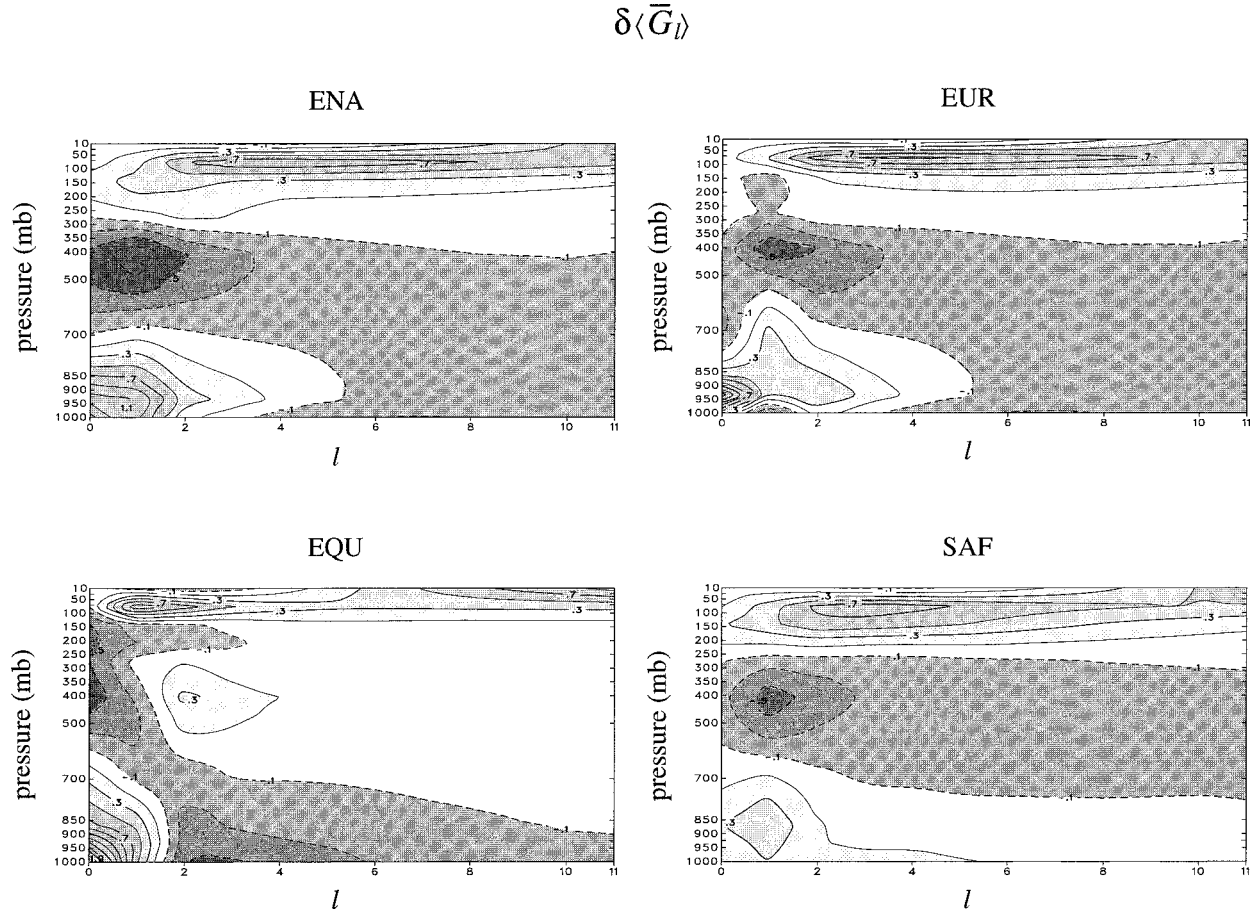
source, dissipated at rate  $D_M$  by mean subgrid vertical mixing (horizontal subgrid-scale mixing is comparatively small and is neglected), and converted at rate  $C$  to eddy tracer variance,  $A_T$ , which is dissipated at rate  $D_T$  by transient subgrid mixing. Note that the integrated variance budget does not depend explicitly on the mean flow, which only acts to redistribute the variance components without changing their global integrals.

Equations (15)–(19) apply to variance budgets integrated over the mass of the atmosphere, but here we confine our interest to the troposphere below 500 mb and evaluate the terms for this region. Formally, the budget for the lower half of the atmosphere includes boundary terms representing interactions with the upper half. However, for constant sources, the generation and dissipation of variance is dominated by processes in the lower half of the atmosphere so that these boundary terms may be

neglected to a good approximation. All terms are evaluated from model output except the transient dissipation term,  $D_T$ , which is obtained as a residual (indicated by the dashed arrows in Fig. 16).

Figure 16 gives the terms in the variance budget for each of the sources for the current climate and the percentage change for the future climate. There is a general increase in all terms. The results for the variance budget reinforce what has been seen previously. The longer transport timescales in the warmer climate result in a buildup of tracer in the vicinity of the source (increasing  $H_M$ ) and a reduction at a distance from the source (Figs. 9–10) so that the gradients of  $\bar{\chi}$ , and hence  $A_M$ , both increase. The change  $\delta C$  in the conversion from mean to eddy variance depends on changes in both the eddy fluxes and mean tracer gradients that we represent as

$$\delta C = \delta C_{\chi'} + \delta C_{\bar{\chi}} \equiv - \int [\delta(\bar{\chi}' \nabla' \cdot \nabla + \bar{\chi}' \omega' \partial_p) \bar{\chi}_1 + (\bar{\chi}' \nabla' \cdot \nabla + \bar{\chi}' \omega' \partial_p)_2 \delta \bar{\chi}] dM. \quad (20)$$



The first term is the change in conversion rate due to the change in eddy transports operating on current (subscript 1) tracer gradients. This term is expected to decrease because of the weaker eddies in the warmer climate and generally does so (Fig. 16), thereby allowing mean gradients to strengthen. The second term gives the effect of changes in the mean gradient of tracer operated on by the eddy fluxes of the warmer climate (subscript 2). This term is positive and larger than the first term so that the change in conversion rate is dominated by the change in mean tracer gradient in the presence of weaker eddy fluxes. Although the transient eddies have weakened, they operate on a stronger tracer gradient to produce an increase in the conversion rate and the transient tracer variance.

An analogous decomposition is applied to the mean dissipation term,  $\delta D_M = \delta D_f + \delta D_{\bar{\chi}}$ , where the vertical subgrid flux  $f$  appears in place of the eddy fluxes. The percentage changes in these components can be large because the term itself is comparatively small (e.g., for the SAF source). The same general result is seen: the change in the mixing due to  $f$  acts to reduce  $D_M$ , while the change in the mean gradient generally acts to increase  $D_M$ .

In this view, the warmer climate is characterized by

larger mean and transient tracer variances in the lower troposphere as a consequence of weaker eddy and sub-grid parameterized vertical transports, which allow the constant source to generate larger gradients. The increased gradients dominate the variance budget and the terms in the budget generally increase.

## 6. Summary and conclusions

Global warming as projected by the CCCma model leads to less vigorous atmospheric flow resulting in longer interhemispheric exchange times, transit times, and mixing times. The magnitude of the changes is about 10%, the same order of magnitude as the changes projected for other climate variables (e.g., Branscome and Gutowski 1992; Coleman et al. 1994; Boer 1995; Carnell and Senior 1998). The slower transport rates of the future climate have implications for the stationary-state structure of long-lived passive tracers with surface sources: The future climate features larger tracer burdens in the source hemisphere and plumes of enhanced mixing ratio ( $\sim 10\%$ ) at low levels downwind from the source. The stationary-state tracer structure with constant sources has weaker gradients across the tropopause



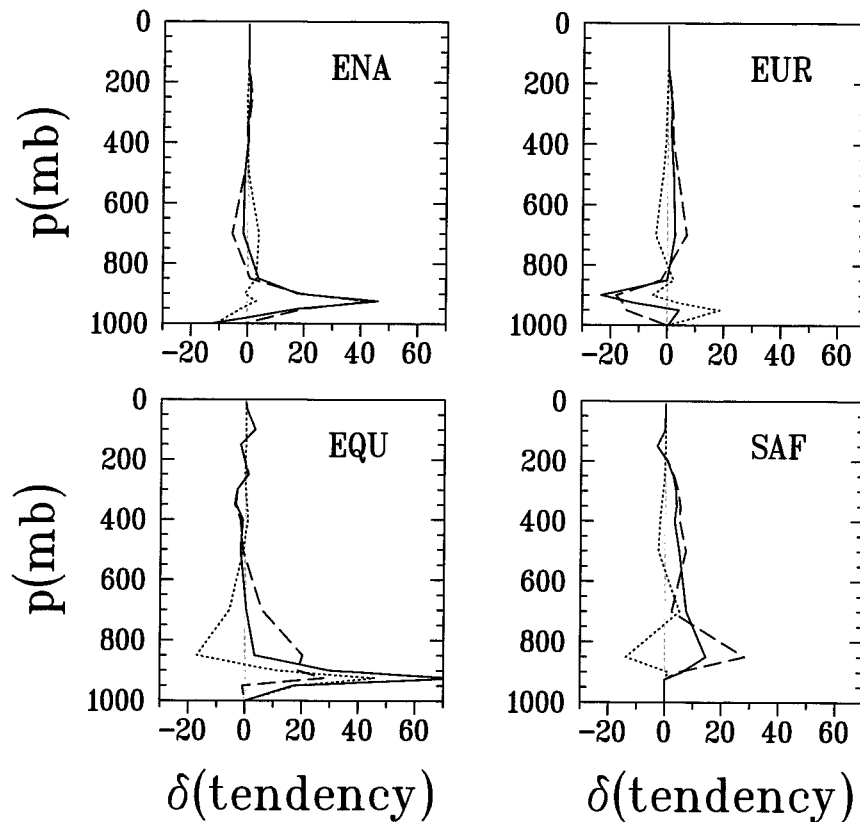


FIG. 15. Vertical profiles of the changes under global warming in the advective tendency  $\delta\bar{A}$  (dotted), in the subgrid tendency  $\delta\bar{D}$  (dashed), and in their sum  $\delta(\bar{A} + \bar{D})$  (solid), as computed for  $\bar{G}_l$  at the four source locations for the month during which the source is on ( $l = 0$ ). The tendencies are in units of  $10^{-6} G_s \text{ s}^{-1}$ .

in the warmer climate. The departure of the mixing ratio from the spatially uniform growing background value broadly decreases ( $\sim 25\%$ ) in the troposphere while increasing ( $\sim 10\%$ ) in the stratosphere. This effect can be understood as resulting from a small increase in the height of the tropopause, which is illustrated using a two-box model of stratosphere–troposphere exchange.

Simulations of pulsed sources are used to cast the transport problem for constant sources in terms of the tracer Green function  $G$  (Holzer 1999). The evolution of  $G$  shows that the near-source enhancement of tracer mixing ratio is associated with the early time (1–2 months) structures of  $G$ . The evolution of  $G$  also demonstrates an  $\sim 10\%$  decrease of the fluxes in the “tracer fountain,” the main transport pathway for interhemispheric exchange. A detailed examination of the terms governing the evolution of  $G$  shows that for different source locations, the near-source tracer enhancement results from differing, and sometimes opposing, contributions from resolved advection and subgrid transport.

Terms in the budget of mean and transient tracer variance all increase in the warmer climate, driven by an increase in the generation of mean variance associated

with enhanced tracer concentration and gradients near the source. Weakened downgradient eddy transport and weakened mean dissipation help maintain mean tracer gradients.

Although climate change is most commonly thought of in terms of changes to primary climatological fields such as surface temperature and precipitation, there will be associated changes in all atmospheric and oceanic variables. The simulated changes in passive tracer transport and distribution investigated here give some indication of the potential change in “transport climate” that may affect trace gases, particulates, and pollutants in the atmosphere under global warming.

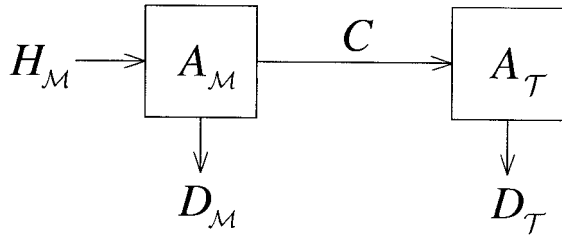
## APPENDIX

### Synthesis of Mixing Ratio from the Mean Green Function

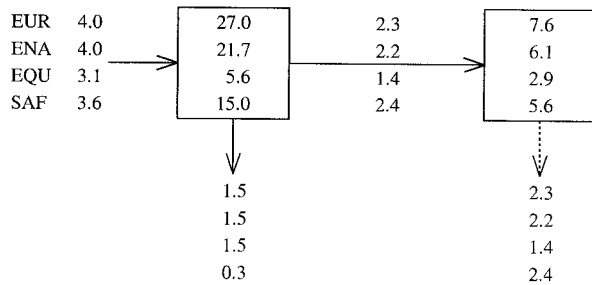
When consecutively lagged mean Green functions  $\bar{G}_l$ , as defined through (7), are superposed one obtains an averaged mixing ratio  $\hat{\chi}$ :

$$M_0 \sum_{l=0}^L \bar{G}_l = \frac{1}{12} \sum_{n=n_0}^{n_0+11} \chi_n(L) \equiv \hat{\chi}(L), \quad (\text{A1})$$

## Tracer Variance Budget



### Current Climate



### Percentage Change

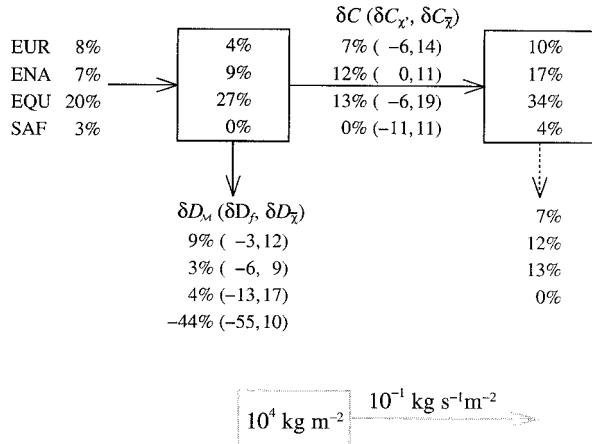


FIG. 16. Terms in the tracer variance budget as defined and discussed in section 5. Values are given for each of the four source cases for the current climate together with the percentage changes under global warming. The dashed arrows indicate that  $D_T$  is obtained as a residual. To scale out the source strength, values are given for the normalized mixing ratio,  $\chi^+/(M_0 G_\infty)$ .

where  $\chi_n(L)$  is the monthly mean mixing ratio obtained with a continuous source switched “on” at the beginning of month  $n - L$  as in (6). Thus,  $\hat{\chi}$  has the interpretation of an average over 12 tracers, each resulting from a continuous source switched on  $L$  months pre-

viously, with the switch-on time being a different month of the year for each of the 12 tracers.

The (standard) annual mean of a single tracer in statistical equilibrium with a continuous source can similarly be synthesized using  $\bar{G}_l$  as defined in (7). This annual mean is given by  $\bar{\chi}(L) \equiv (1/12) \sum_{m=0}^{11} \chi_{n+m}(L + m)$  for mixing ratio resulting from a continuous source switched on  $L$  months ago. Substituting the decomposition  $\chi_n(L) = \chi_n^+ + \chi_n^0(L) = \chi_n^+ + (L + 1/2)M_0 G_\infty$  into (A1), one immediately obtains (8), namely,

$$\bar{\chi}^+ = M_0 \sum_{l=0}^{\infty} (\bar{G}_l - G_\infty) + \frac{1}{2} M_0 G_\infty, \quad (\text{A2})$$

where  $\bar{\chi}^+ \equiv (1/12) \sum_{m=0}^{11} \chi_{n+m}^+$ , we again suppress the dependence of  $\bar{\chi}^+$  on  $n$  assuming negligible interannual fluctuations of the annual mean, and we have taken the long-time limit,  $L \rightarrow \infty$ , to ensure equilibrium. [The added  $(1/2)M_0 G_\infty$  in (8) is due to  $\chi_n^0(L)$  being the *monthly average* of  $\chi^0$  and not its instantaneous value after  $L + 1$  months of constant source.] In practice the sum (8) converges rapidly in the troposphere (Holzer 1999). Since equilibrium for the tracer here means that the source has been on for long enough so that  $\chi_n^+$  is independent of  $L$ , we note for completeness that in equilibrium (large  $L$ ), the averages  $\bar{\chi}(L)$  and  $\hat{\chi}(L)$  differ merely by a constant offset, that is,  $\bar{\chi}(L) = \hat{\chi}(L) + (11/2)M_0 G_\infty$ .

### REFERENCES

- Boer, G. J., 1995: Some dynamical consequences of greenhouse gas warming. *Atmos.–Ocean*, **33**, 731–751.
- , G. Flato, and D. Ramsden, 2000a: A transient climate change simulation with greenhouse gas and aerosol forcing: Projected climate for the twenty-first century. *Climate Dyn.*, **16**, 427–450.
- , —, M. C. Reader, and D. Ramsden, 2000b: A transient climate change simulation with greenhouse gas and aerosol forcing: Experimental design and comparison with the instrumental record for the twentieth century. *Climate Dyn.*, **16**, 405–425.
- Bowman, K. P., and P. J. Cohen, 1997: Interhemispheric exchange by seasonal modulation of the Hadley circulation. *J. Atmos. Sci.*, **54**, 2045–2059.
- Branscome, L. E., and W. J. Gutowski, 1992: The impact of double CO<sub>2</sub> on the energetics and hydrological processes of mid-latitude transient eddies. *Climate Dyn.*, **7**, 29–37.
- Carnell, R. E., and C. A. Senior, 1998: Changes in mid-latitude variability due to increasing greenhouse gases and sulphate aerosols. *Climate Dyn.*, **14**, 369–383.
- Coleman, R. A., B. J. McAvaney, J. R. Fraser, and S. B. Powers, 1994: Annual mean meridional energy transport modelled by a general circulation model for present and  $2 \times \text{CO}_2$  equilibrium climates. *Climate Dyn.*, **10**, 221–229.
- Cubash, U., and Coauthors, 2001: Projections of future climate change. *Climate Change 2001: The Scientific Basis, Contribution of Working Group I to the Third Assessment Report of the Intergovernmental Panel on Climate Change*, J. T. Houghton et al., Eds., Cambridge University Press, 944 pp.
- Flato, G. M., G. J. Boer, W. Lee, N. McFarlane, D. Ramsden, M. C. Reader, and A. Weaver, 2000: The Canadian Centre for Climate Modelling and Analysis global coupled model and its climate. *Climate Dyn.*, **16**, 451–467.
- Hall, N. M., B. J. Hoskins, P. J. Valdes, and C. A. Senior, 1994: Storm tracks in a high-resolution GCM with double carbon dioxide. *Quart. J. Roy. Meteor. Soc.*, **120**, 1209–1230.

- Hall, T. M., and R. A. Plumb, 1994: Age as a diagnostic of stratospheric transport. *J. Geophys. Res.*, **99**, 1059–1070.
- , D. W. Waugh, K. A. Boering, and R. A. Plumb, 1999: Evaluation of transport in stratospheric models. *J. Geophys. Res.*, **104**, 18 815–18 839.
- Holzer, M., 1999: Analysis of passive tracer transport as modeled by an atmospheric general circulation model. *J. Climate*, **12**, 1659–1684.
- , and T. M. Hall, 2000: Transit-time and tracer-age distributions in geophysical flows. *J. Atmos. Sci.*, **57**, 3539–3558.
- Lambert, S. J., 1995: The effect of enhanced greenhouse warming on winter cyclone frequencies and strengths. *J. Climate*, **8**, 1447–1452.
- Law, R. M., and Coauthors, 1996: Variations in modelled atmospheric transport of carbon dioxide and the consequences for CO<sub>2</sub> inversions. *Global Biogeochem. Cycles*, **10**, 483–496.
- McFarlane, N. A., G. J. Boer, J.-P. Blanchet, and M. Lazare, 1992: The Canadian Climate Centre second generation general circulation model and its equilibrium climate. *J. Climate*, **5**, 1013–1044.
- Meehl, G. A., W. D. Collins, B. A. Boville, J. T. Kiehl, T. M. L. Wiegly, and J. M. Arblaster, 2000: Response of the NCAR climate system model to increased CO<sub>2</sub> and the role of physical processes. *J. Climate*, **13**, 1879–1898.
- Morse, P. M., and H. Feshbach, 1953: *Methods of Theoretical Physics*. McGraw-Hill, 997 pp.
- Plumb, R. A., and J. D. Mahlman, 1987: The zonally averaged transport characteristics of the GFDL general circulation/transport model. *J. Atmos. Sci.*, **44**, 298–327.
- , and D. D. McConalogue, 1988: On the meridional structure of long-lived tropospheric constituents. *J. Geophys. Res.*, **93**, 15 897–15 913.